

NASA Contractor Report 172225

NASA-CR-172225
19840005539

THREE-DIMENSIONAL ANALYSIS OF CHEVRON-NOTCHED
SPECIMENS BY BOUNDARY INTEGRAL METHOD

FOR REFERENCE

NOT TO BE TAKEN FROM THIS ROOM

Alexander Mendelson and Louis Ghosn

CASE WESTERN RESERVE UNIVERSITY
Cleveland, Ohio 44106

Grant NAG1-304
September 1983

LIBRARY COPY

DEC 8 1983

LANGLEY RESEARCH CENTER
LIBRARY, NASA
HAMPTON, VIRGINIA



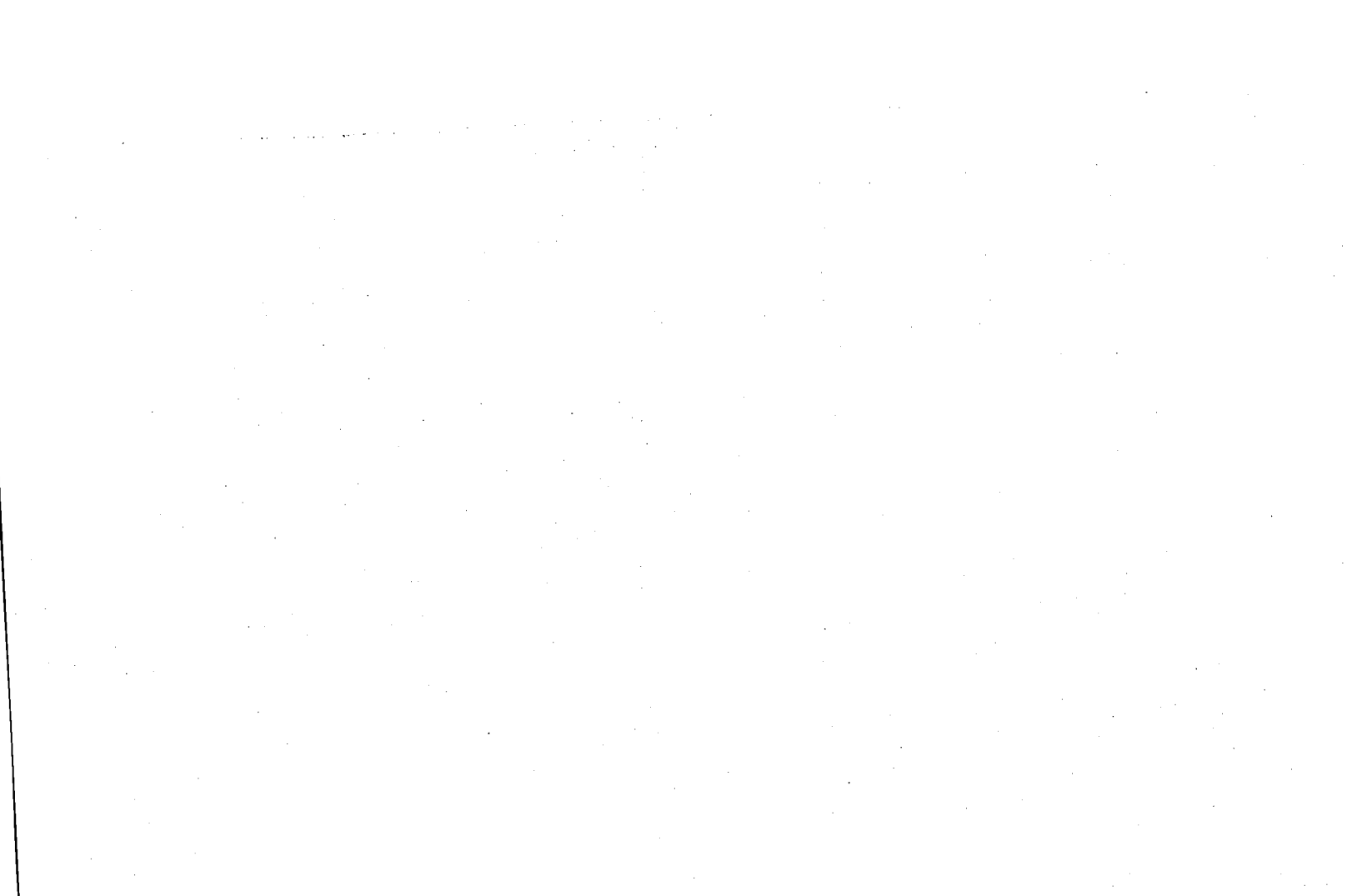
National Aeronautics and
Space Administration

Langley Research Center
Hampton, Virginia 23665

recorded with an eight channel waveform digitizer capable of sampling data
ENTER:

26. 1 1 RN/NASA-CR-172225
DISPLAY 26/2/1
84N13607*# ISSUE 4 PAGE 547 CATEGORY 39 RPT#: NASA-CR-172225 NAS
1.26:172225 CNT#: NAG1-304 83/09/00 107 PAGES UNCLASSIFIED DOCUMENT
UTTL: Three-dimensional analysis of chevron-notched specimens by boundary
integral method TLSP: Final Report
AUTH: A/MENDELSON, A.; B/GHOSH, L.
CORP: Case Western Reserve Univ., Cleveland, Ohio. CSS: (Dept. of Civil
Engineering.) AVAIL. NTIS SAP: HC A06/MF A01
MAJS: /*BOUNDARY INTEGRAL METHOD/*CERAMICS/*DISPLACEMENT MEASUREMENT/*FRACTURE
MECHANICS
MINS: / ELASTIC PROPERTIES/ MECHANICAL PROPERTIES/ STRESS INTENSITY FACTORS
ABA: E. A. K.
ABS: The chevron-notched short bar and short rod specimens was analyzed by the
boundary integral equations method. This method makes use of boundary
surface elements in obtaining the solution. The boundary integral models
were composed of linear triangular and rectangular surface segments.
Results were obtained for two specimens with width to thickness ratios of
1.45 and 2.00 and for different crack length to width ratios ranging from
0.4 to 0.7. Crack opening displacement and stress intensity factors
determined from displacement calculations along the crack front and
compliance calculations were compared with experimental values and with
finite element analysis.

ENTER



THREE-DIMENSIONAL ANALYSIS OF CHEVRON-NOTCHED SPECIMENS

BY BOUNDARY INTEGRAL METHOD

Abstract

by

Alexander Mendelson and Louis Ghosn

A three-dimensional elastic analysis was performed on the chevron-notched short-bar and short-rod specimens, using the boundary integral equations method. This method makes use of boundary surface elements in obtaining the solution. The boundary integral models were composed of linear triangular and rectangular surface segments. Results were obtained for two specimens with width-to-thickness ratios of 1.45 and 2.00 and for different crack-length-to-width ratios ranging from 0.4 to 0.7. Crack opening displacement, and stress intensity factors determined both from displacement calculations along the crack front and compliance calculations were compared with experimental values obtained at NASA Lewis research Center, and with finite-element analysis done at NASA Langley Research Center.

TABLE OF CONTENTS

	Page
ABSTRACT	i
TABLE OF CONTENTS	iii
LIST OF TABLES	v
LIST OF FIGURES	vi
LIST OF SYMBOLS	ix
CHAPTER I INTRODUCTION	1
CHAPTER II CHEVRON-NOTCHED SPECIMEN	10
2-1 Introduction	10
2-2 Stability Analysis	11
2-3 Determination of Stress Intensity Factor	15
2-4 Compliance Calibration	17
2-5 Stress and Displacement Fields	19
CHAPTER III THREE-DIMENSIONAL BOUNDARY INTEGRAL EQUATIONS METHOD	21
3-1 Introduction to the Boundary Integral Methods	21
3-2 Mathematical Derivation	22
CHAPTER IV NUMERICAL PROCEDURE	28
4-1 Reduction of the Integral Equations To a Set of Simultaneous Equations	28
4-2 Single-Edge-Cracked Tension Specimen	36
4-3 Discretization of the Chevron-Notched Specimens	45

CHAPTER V	RESULTS AND DISCUSSION FOR THE SHORT-BAR AND SHORT-ROD	65
	5-1 Stress Intensity Factor from Compliance	69
	5-2 Stress Intensity Along the Crack Front	74
CHAPTER VI	CONCLUSIONS	84
REFERENCES		86
APPENDIX A	Derivation of the Singular Integral	88
APPENDIX B	Numerical Solution of the Integral Equations	92
APPENDIX C	Program Listing	96

LIST OF TABLES

Table		Page
1	Normalized stress intensity factor for SECT specimen	38
2	Crack mouth opening displacement for different meshes	48
3	Summary of specimen dimensions	65
4	Normalized crack opening displacement for Chevron-notched specimens as function of a/W	68
5	Typical variation of the displacement at the center the specimen to its outer surface along the loading line	70
6	Normalized average displacement along the loading line, EVB/p	70
7	Coefficients of the least square fit of the compliance	71
8	Critical stress intensity factor for the Chevron-notched specimens	72
9	Comparison between the minimum stress intensity factor assuming plane stress condition	74
10	Stress intensity factor, y^* , along the crack front for the short-bar specimens	75
11	Stress intensity factor, y^* , along the crack front for the short-rod specimens	76

LIST OF FIGURES

<u>Figure</u>		<u>Page</u>
1.	Crack in an infinite plate under uniform stress condition	2
2.	Different specimens for fracture toughness testing	5
3.	Chevron-Notched short-bar and short-rod specimens	6
4.	a) Side-view of the Chevron-notched specimen	12
	b) Section-view of the plane of the chevron notch	12
	c) Load versus opening displacement of the chevron-notched specimens	12
5.	Point load in an infinite region	23
6.	Typical surface mesh for constant segment	30
7.	Linear segments	32
8.	Intersection of two segments that lie in different planes	32
9.	Segment free crack front	34
10.	Parabolic segment for discontinuity regions	34
11.	Special constant segment	35
12.	Single-edge-cracked-tension specimen	39
13.	Stress distribution at the centerline of the SECT specimen	40
14.	Displacement distribution at the centerline of the SECT specimen	41
15.	V/\sqrt{r} versus r for the two meshes of the SECT specimen	42
16.	Variation of V/\sqrt{r} along the crack front for SECT	43

<u>Figure</u>		<u>Page</u>
17.	Normalized stress intensity factor for the SECT specimen	44
18.	Chevron-notched bar specimen	51
19.	Loading condition for the chevron notch specimen	52
20.	Mesh 1 with 61 nodes for $a/W = 0.4$	53
21.	Mesh 2 with 221 nodes for $a/W = 0.4$	54
22.	Mesh 3 with 370 nodes for $a/W = 0.4$	55
23.	Crack opening displacement as function of a/W	56
24.	Crack opening displacement as function of nodes for $a/W = 0.4$	57
25.	Mesh 4 with 370 nodes for $a/W = 0.5$	58
26.	Normalized crack opening displacement as function of a/W	59
27.	Normalized displacement distribution at the centerline of the short-bar specimen for $a/W = 0.5$	60
28.	Normalized stress intensity factor as function of a/W (from compliance)	61
29.	Variation of V/\sqrt{r} for the chevron notch bar specimen for $a/W = 0.5$	62
30.	Variation of the stress intensity factor along the crack front for different mesh for $a/W = 0.5$	63
31.	Variation of the stress intensity factor at the centerline of the specimen for $a/W = 0.5$ as function of the number of nodes	64
32.	End-view of the short-bar and short-rod specimens	67

<u>Figure</u>		<u>Page</u>
33.	Stress intensity factor from compliance for the chevron notched specimens as function of a/W	73
34.	Variation of the stress intensity factor along the crack front of the short-bar specimen with $W/B = 1.45$	71
35.	Variation of the stress intensity factor along the crack front of the short-bar specimen with $W/B = 2.00$	80
36.	Variation of the stress intensity factor along the crack front of the short-rod specimen with $W/B = 1.45$	81
37.	Variation of the stress intensity factor along the crack front of the short-rod specimen with $W/B = 2.00$	82
38.	Propagation of the crack front for the short-rod specimen Ref. [11]	83

LIST OF SYMBOLS

a	Crack length
a_0	Distance between the load line to the apex of the triangular ligament
a_1	Distance between the load line to the base of the triangular ligament
a_c	Critical crack length where the stress intensity factor goes through a minimum
A	Geometric correction factor for the chevron-notched specimen at the critical stress intensity factor
b	crack width ($b = B \frac{a - a_0}{a - a_1}$ for the chevron notch)
B	Specimen width
B_i	Coefficients of the parabolic fit for the compliance
C	Compliance ($C = \frac{V}{P}$)
C^*	Normalized compliance ($C^* = \frac{E'VB}{P}$)
C^K	Coefficient of variation for the triangular segments
C_{ij}	Solution of the integral at singularity points
d_i	Coefficient of the least square fit for the compliance
e_i	Component of the unit vector in the i direction
E	Modulus of elasticity
E'	$= E$ for plane stress $= \frac{E}{1 - \nu^2}$ for plane strain
F_{ki}	Projections of the distance between two adjacent nodes in local coordinates for triangular segments
G	Shear modulus

G_I	Strain energy release rate
G_{IC}	Critical strain energy release rate
H	Half the specimen height
K_I	Stress intensity factor
K_{IC}	Critical stress intensity factor
n_j	Component of the outward normal in j direction
N^K	Component for variation coefficient for rectangular segments
O	Higher order terms
P	Total load applied
P_{MAX}	Maximum load
Q	Field point at the boundary of the specimen
r	Distance to the crack tip
R	Infinite region
S_i	Variation coefficient for the parabolic segments
S_n	Surface segment
S	Boundary surface
t_j	Traction component
T_{ij}	Traction solution due to a point load in an infinite region
T_{ijk}	Stress component for a point load
u_j	Traction component
U	Elastic strain energy
U_{ij}	Displacement solution for a point load in an infinite region
V	Total displacement in y direction
W	Specimen length
W_L	Work done by external forces
x'	Distance between the end of the specimen to the loading line

y'	Distance between the load line to the end of the groove
y^*	Normalized stress intensity factor
y_m	Minimum stress intensity factor
X,Y,Z	Global coordinate system
x,y,z	In-plane local coordinate system
α_i	$= \frac{a_i}{W}$
δ_{ij}	Chronical delta
ϵ	Small radius of a sphere around the singularity point
θ	$= u_{j,j}$
σ_i	Normal stresses
σ_{ij}	Stress tensor
τ_{ij}	Shear stress
ξ	Local in-plane coordinates for the triangular segments
ξ_m	Local coordinate of the center of the triangular segment
ν	Poisson's ratio
BIE	Boundary Integral Equations
CMOD	Crack Mouth Opening Displacement
FEM	Finite Element Method
MOL	Method Of Line
SECT	Single-Edge-Crack-Tension specimen
SIF	Stress Intensity Factor

CHAPTER I

Introduction

The outstanding physical properties of ceramic materials from high temperature strength and corrosion resistance, to low density and low thermal conductivity has stimulated interest in manufacturing ceramic materials for high temperature structural applications. As an example, a gas turbine with ceramic components, could operate at higher temperatures than metallic components, thus improving the overall efficiency of power generation, and reducing fuel consumption.

Design criteria for ceramic structures are very complicated due to the great amount of data scatter encountered in the fracture strength of the same material, and due to low resistance to failure in the presence of defects, as compared to structural metals of similar strength levels. The inherent brittleness of ceramic materials allows no plastic flow to occur to relieve the high stress. Therefore, very small flaws (0.001 in. or less) can create very high localized stresses at crack tips. When the local stress level reaches the inherent strength of the material, failure occurs. This failure concept can be analyzed using linear elastic fracture mechanics, since the basic concepts in

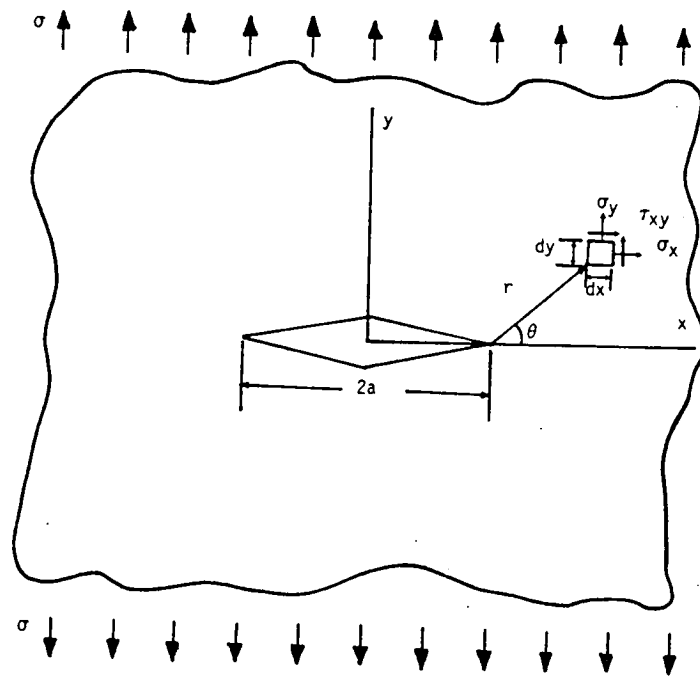


Figure 1. Crack in an infinite plate under uniform stress condition

fracture mechanics were derived from perfect linear elastic inherently brittle material behavior.

The presence of a flaw of length $2a$ in a ceramic structural component, loaded with a force P , creates high stress gradients near the crack tip. Considering the two dimensional solution for an infinite plate with applied stress σ normal to the crack plane, the stress distribution near the crack tip can be shown to be [1]

$$\sigma_y = \frac{\sigma\sqrt{a}}{\sqrt{2r}} \cos \frac{\theta}{2} \left[1 + \sin \frac{\theta}{2} \sin \frac{3\theta}{2} \right] + O \left[r^{1/2} \right]$$

$$\sigma_x = \frac{\sigma\sqrt{a}}{\sqrt{2r}} \cos \frac{\theta}{2} \left[1 - \sin \frac{\theta}{2} \cos \frac{3\theta}{2} \right] + O \left[r^{1/2} \right]$$

$$\tau_{xy} = \frac{\sigma\sqrt{a}}{\sqrt{2r}} \sin \frac{\theta}{2} \cos \frac{\theta}{2} \cos \frac{3\theta}{2} + O \left[r^{1/2} \right]$$

where r and θ are the polar coordinates of a point measured from the tip of the crack (Figure 1). Linear fracture mechanics defines the opening mode stress intensity factor (K_I) as

$$\lim_{\substack{r \rightarrow 0 \\ \theta = 0}} \sigma_y \sqrt{2\pi r} = K_I$$

For an infinite plate $K_I = \sigma \sqrt{\pi a}$ and in general for a finite plate of a particular geometry $K_I = Y \sigma \sqrt{a}$ where Y is a geometric correction factor. Similarly for wedge loading the

opening mode stress intensity factor can be expressed as $K_I = \frac{Y P}{B \sqrt{W}}$, where W is the distance between the crack tip and position of the load P while B is the width of the specimen.

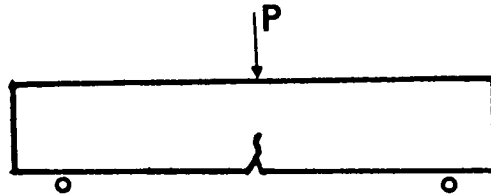
It is assumed that beyond a critical value of the stress intensity factor ($K_I > K_{IC}$) the crack will propagate. The fracture toughness (K_{IC}) is defined as an inherent material strength property which refers to the resistance of a material to fracture in the presence of a flaw. The value of K_{IC} can be determined only experimentally.

There exists no standard test for the determination of fracture toughness (K_{IC}) of brittle non metallic materials. The test specimens that have been used in ceramic materials testing can roughly be divided into five groups (Figures 2 and 3).

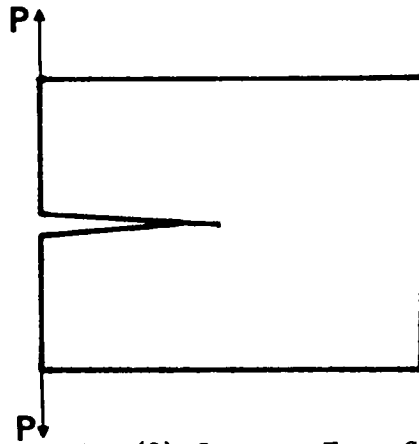
1. Bent Bar.
2. Compact type.
3. Double cantilever beam.
4. Controlled surface flaw.
5. Short-bar and short-rod chevron-notched.

The first four specimens have either blunt notches produced by sawcutting or cracks produced by wedge loading. Specimens with blunt notches can overestimate K_{IC} . Precracked specimens are difficult to prepare in a reproducible manner, and it is relatively difficult to monitor the crack length and the crack growth rate.

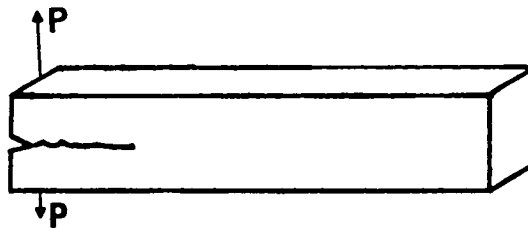
To overcome these difficulties Barker [2] has proposed a



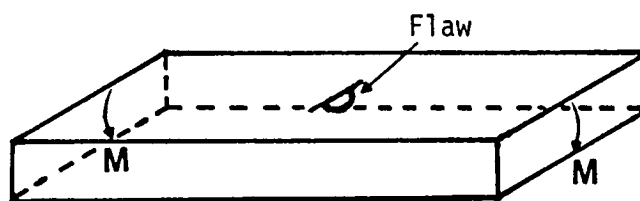
(1) Bend Bar Specimen



(2) Compact Type Specimen



(3) Double Cantilever Beam Specimen



(4) Controlled Surface Flaw Specimen

Figure 2. Different specimens for fracture toughness testing

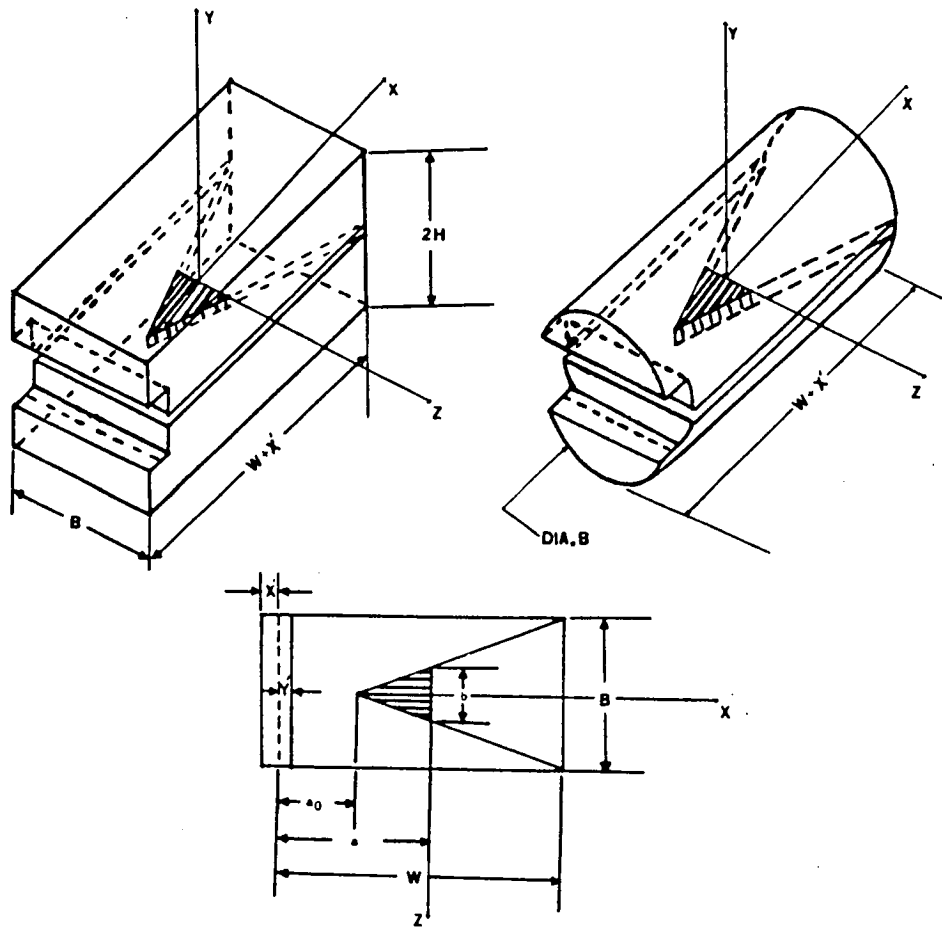


Figure 3. Chevron-Notched short-bar and short-rod specimens

specimen with a chevron-notch, as shown in Figure 3, in which a crack always originates at the tip of the triangular notch during loading. The crack growth has been found to be stable since it requires an increasing load for continued crack advance until the crack length reaches a critical value a_c where the load goes through a smooth maximum. The fracture toughness K_{IC} is determined from the peak load P_{MAX} and the specimen geometry. The measurement of the crack length is not necessary.

Taking into consideration the advantages of the chevron-notch specimen, the American Society for Testing and Materials Committee E24 has been considering this type of specimen for standardization to determine the plane strain fracture toughness of brittle non-metallic materials. For the universal application of the short-bar and short-rod specimens the relation between K_I , P_{MAX} and Y must be known. This requires a three-dimensional analysis and/or an experimental compliance calibration of this relatively complex geometry.

Extensive experimental compliance calibrations of the short-bar and short-rod specimens had been carried out by Barker [3] [4], Barker and Guest [5], Munz et.al. [6], Budsey et.al. [7] and Shannon et. al. [8]. To back the experimental results a rigorous stress analysis is needed to determine the stress and displacement distributions in the vicinity of the crack-tip of the chevron-notch specimens.

Some numerical calibration of short-bar and short-rod

specimens had been performed and presented at the ASTM Symposium on Chevron-Notched Specimens: Testing and Stress-Analysis, on April 21, 1983, in Louisville, Kentucky. Raju and Newman [9] presented their calibrations of the short-bar and short-rod specimens calculated by a three-dimensional finite element analysis. Mendelson and Ghosn [10], as part of the investigation described herein, presented one calibration of a short-bar specimen with width-to-thickness ratio equal to 2.0, using the boundary integral methods. Ingraffea et.al. [11] presented results using both numerical methods on the short-rod with width to thickness ratio equal to 1.45.

The purpose of this work is to present numerical calibrations of the chevron-notched short-bar and short-rod specimens using the boundary integrals equation method. The crack opening displacement and stress-intensity factor calculated from the displacement distribution along the crack front and the compliance method will be presented. The dimensions used for the specimens were the ones suggested by ASTM E24.01.05 Task Group with two width-to-specimen thicknesses of 1.45 and 2.0, and different crack-length-to-width ratios ranging from 0.4 to 0.7.

A complete analysis of the chevron-notched specimens is given in Chapter II of this report. The derivation of the stability analysis for this notched geometry is also given with a review of the different methods to determine the stress intensity factor.

Chapter III is concerned with the boundary integral equations

method and its mathematical derivations. Chapter IV deals with the numerical procedures for this method. In that Chapter several mesh sizes were used to determine the effect of mesh sizes on the stress intensity factor. To check the equations and computer program, the single-edge-cracked tension specimen is analyzed, since the results for the SECT were available by other methods.

Finally in Chapter V the stress intensity factors for the chevron-notched short-bar and short-rod are presented. The results from the compliance calibration method (see Chapter II Section 2.4) and from displacements near the crack tip are compared. And finally the calibration constant Y^* for different specimen geometries at the critical crack length is determined.

CHAPTER II

Chevron-notched specimen

2.1 Introduction

For extremely brittle materials, such as ceramics, experimental results to determine the fracture toughness using a conventional straight thru crack are very difficult to obtain. A ceramic specimen containing a blunt notch usually overestimates the fracture toughness. Attempts to introduce a sharp crack by fatigue or local thermal-shock in a reproducible manner are very difficult. Furthermore, the initial crack front often cannot be seen on the fracture surface after testing, making it impossible to measure the initial crack length required to measure the fracture toughness.

An alternative to the conventional straight thru notch is the chevron or V notch, first used by Tattersall and Tappin [12] in their bending tests. Two inclined cuts are put into the specimen such that the remaining ligament is an isosceles triangle. When a small load is applied, a stress concentration of sufficient magnitude exists at the apex of the triangle to initiate a sharp stable crack. Barker [2] applied this notch geometry to double cantilever type specimens called short-bar and short-rod (see

Figure 3). He found that this configuration exhibits an initial crack growth stability up to a critical crack length a_c , independent of material properties. At this point the load versus opening displacement curve goes thru a smooth maximum, and then the crack growth will become unstable (see Figure 4). Such a specimen configuration, once calibrated, can be used for fracture toughness tests, in which the only measured parameter is the peak force. A theoretical review of the stability and calibration procedure for the chevron-notch specimens is discussed in the next sections.

2.2 Stability Analysis

The strain energy release rate, G_I , is defined as the mechanical energy released during an incremental crack area extension

$$G_I = \frac{d(W_L - U)}{dS} \quad (2.1)$$

W_L is the work done by external forces and U is the elastic strain energy. For elastic materials G_I is equal to (Figure 4)

$$G_I = \frac{1}{2} \frac{P^2}{b} \frac{dC}{da} \quad (2.2)$$

where d = Derivative

p = total load

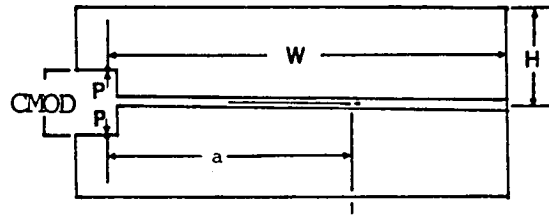


Figure 4. a) Side-view of the Chevron-notched specimen

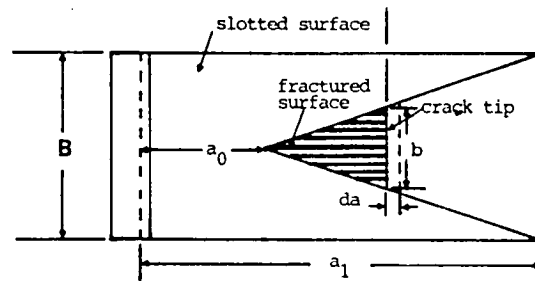


Figure 4. b) Section-view of the plane of the chevron notch

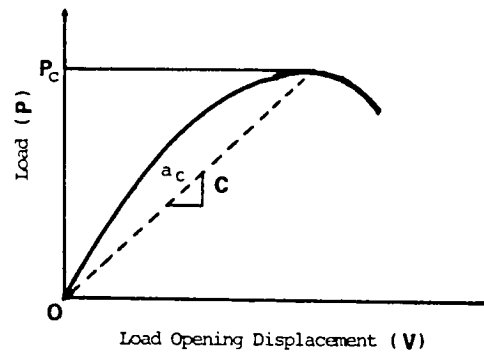


Figure 4. c) Load versus Opening displacement of the chevron-notched specimens

b = crack width ($b=B$ for straight thru crack)

$$\left(b=B \frac{a-a_0}{a_1-a_0} \right) \quad \text{for chevron-notch}$$

B = thickness of specimen

$$C = \text{compliance} = \frac{V}{P}$$

V = opening displacement under load $P=\Delta\text{CMOD}$

From linear elastic fracture mechanics, where a plane strain condition exists in the vicinity of the crack tip, the crack will not advance if

$$G_I < G_{IC} \quad (2.3)$$

where G_{IC} is the plane strain critical energy release rate. If the inequality is satisfied the crack is said to be stable. Substituting the value of G_I from eq (2.2), (2.3) becomes

$$\frac{1}{2} P^2 \frac{dc}{da} < G_{IC} \cdot b \quad (2.4)$$

Inequality (2.4) is the well known condition for crack position stability.

If we increase P until the left hand side of (2.4) equals the right hand side, the crack will begin to advance. As the crack advances, the inequality (2.4) might be restored since both sides of the above equation might increase. For a straight thru crack b is equal to the specimen width (B) and is constant. Since G_{IC} is assumed to be a material constant, the right hand side of (2.4) cannot increase. However for the chevron-notch, b is not constant and it will increase as the crack length increases. If b increases faster than the left hand side, then the crack growth

will stop. The original inequality will be restored. The condition for stable crack growth of the chevron-notch is then

$$\frac{d}{da} \left[\frac{P}{2} \frac{dC}{da} \right] < \frac{d}{da} [b \cdot G_{Ic}] \quad (2.5.a)$$

for constant P

$$\frac{P}{2} \frac{d^2 C}{da^2} < G_{Ic} \frac{db}{da} \quad (2.5.b)$$

when the cracks start to grow; from eq. (2.4)

$$P^2 = \frac{2 b G_{Ic}}{\frac{dC}{da}}$$

Also, noting that: $\frac{db}{da} = \frac{B}{a_1 - a_0} = \frac{b}{a - a_0}$ (See Figure 4.b), then equation (2.5) becomes :

$$\frac{2 b G_{Ic}}{\frac{dC}{da}} \frac{1}{2} \frac{d^2 C}{da^2} < G_{Ic} \frac{b}{a - a_0} \quad (2.6.a)$$

$$\frac{d^2 C}{da^2} < \frac{\frac{dC}{da}}{a - a_0} \quad (2.6.b)$$

Experiments have shown that the crack will grow in a stable fashion until a critical value $a = a_c$ is reached. At $a = a_c$ the crack growth will become unstable, i.e. the crack will then propagate until the specimen fractures. Since inequality (2.6) is satisfied for $a < a_c$ and not satisfied for $a > a_c$, then at $a = a_c$ we must have

$$\left. \frac{d^2 CE}{da^2} \right|_{a=a_c} = \frac{1}{a_c - a_0} \left. \frac{dCE}{da} \right|_{a=a_c}, \quad (2.7)$$

where both sides were multiplied by the modulus of elasticity, E.

2.3 Determination of Stress Intensity Factor

Consider an experiment in which the load P is slowly increased. The crack length will increase from $a = a_0$, at the tip of the triangular ligament. When the crack length reaches a_c the load will have reached a critical value P_c (See Figure 4.c). From equation 2.4 , we have :

$$\left. \frac{1}{2} P_c^2 \frac{dC}{da} \right|_{a=a_c} = b_c \cdot G_{Ic}$$

Multiplying by EB^3

$$\left. \frac{1}{2} \frac{B^3 E}{b_c} \frac{dC}{da} \right|_{a=a_c} = \frac{G_{Ic} EB^3}{P_c^2} \quad (2.8)$$

Defining A^2 to be equal to the left hand side of equation 2.8 then

$$G_{Ic} = \frac{A^2 P_c^2}{EB^3} \quad (2.9)$$

The critical stress intensity factor K_{Ic} can then be determined from ref [1]

$$G_{Ic} E = K_{Ic}^2 (1 - \nu^2)$$

So equation 2.9 can be written as

$$K_{Ic} = \frac{P_c \cdot A}{B^{3/2} (1 - \nu^2)} \quad (2.10)$$

Barker has shown that A will always be the same independent of material properties, and the absolute size of the specimen. A is shown to be a function of the compliance at the critical crack length a_c . For the sample configuration that Barker had considered, a_c is to a good approximation independent of material properties. Therefore, A is also assumed to be independent of material properties.

Once A is calibrated, to determine K_{Ic} , a short-bar or a short-rod fracture test is performed where the only parameter measured is the maximum load P_c required for failure. To determine the calibration constant A, Barker ran fracture tests with a chevron-notch on materials with well known K_{Ic} . Then he simply determined A by the known value of K_{Ic} , ν and the experimentally measured value of P_c .

For universal application of the short-bar and short-rod specimens, the stress intensity factor should be analyzed using more standardized methods.

In this work, K_I is determined using compliance calculations and the displacement fields along the crack front.

2.4 Compliance Calibration

The compliance calibration test is basically a method to determine the rate of change of the compliance as the crack length increases. If $\frac{dC}{da}$ is known then from equation (2.2), the strain energy release rate can be calculated. What is usually done is to run tests for different crack lengths a , and the load versus displacement is recorded for every crack length. This procedure can be done analytically using the boundary integral equations method. For every crack length position, the opening displacement is calculated for a given load. Since ceramic materials are brittle, the linear elastic assumption is valid; i.e. the compliance is given by $C = \frac{V}{P}$.

The compliance C is plotted as function of crack length, and then fitted by a polynomial. Finally G_I and K_I are determined by differentiating the polynomial.

From equation (2.2)
$$G_I = \frac{1}{2} \frac{P}{b} \frac{dC}{da}$$

Substituting the value of b for a chevron-notch specimen, and defining a new dimensionless variable $\alpha_i = a_i/W$ then eq. (2.2) will have the form

$$G_I = \frac{1}{2} \frac{P}{BW} \frac{\alpha_1^{-\alpha_0}}{\alpha^{-\alpha_0}} \frac{dC}{d\alpha} \quad (2.11)$$

and

$$K_I = \frac{P}{\sqrt{BW}} \left[\frac{1}{2} \frac{\alpha_1 - \alpha_0}{\alpha - \alpha_0} \frac{d CE'}{d \alpha} \right]^{1/2} \quad (2.12)$$

where $E' = E$ for plane stress condition

$$E' = \frac{E}{1-\nu^2} \text{ for plane strain condition}$$

Introducing a dimensionless compliance

$$C^* = CE'B = \frac{E'VB}{P}$$

Then (2.12) becomes

$$K_I = \frac{P}{B\sqrt{W}} \left[\frac{1}{2} \frac{\alpha_1 - \alpha_0}{\alpha - \alpha_0} \frac{dC^*}{d\alpha} \right]^{1/2} \quad (2.13)$$

Munz et.al. [6] defined

$$Y^* = \left[\frac{1}{2} \frac{\alpha_1 - \alpha_0}{\alpha - \alpha_0} \frac{dC^*}{d\alpha} \right]^{1/2}$$

Then equation (2.13) becomes

$$K_I = \frac{P}{B\sqrt{W}} Y^* \quad (2.14)$$

At the critical crack length a_c , comparing eq. (2.14) and eq.(2.10), one gets:

$$A = \sqrt{\frac{B}{W}} \cdot Y^* \Big|_{a=a_c}$$

Thus if Barker had normalized his calibration constant A using $B^2 W$ instead of B^3 , the two geomtric factors A and $Y^* \Big|_{a=a_c}$ would be the same.

2.5 Stress and displacement fields

Since the stress and displacement solutions are provided by the boundary integral equations method, the stress intensity factor can be determined from its basic definition.

$$\lim_{\substack{r \rightarrow 0 \\ \theta = 0}} \sigma_y \sqrt{2\pi r} = K_I \quad (2.15)$$

The stresses, in a region not far from the crack tip, are multiplied by the square root of the distance x from the crack front, then plotted versus x . A curve is then fitted thru those points, where its value at x equal zero is proportional to K_I .

Alternatively, the displacements could be used, by noting that

$$\lim_{\substack{r \rightarrow 0 \\ \theta = \pi}} \frac{V \cdot \sqrt{2\pi E}}{\alpha \cdot \sqrt{r}} = K_I \quad (2.16)$$

Now the displacement divided by \sqrt{x} is plotted versus x , and the intersection of this curve at $x = 0$ is proportional to K_I . Using

the displacements, an unknown parameter α is introduced. For plane strain condition α is assumed to be equal to $4(1-\nu^2)$, and for plane stress α is equal to 4.

Determining the stress intensity factor, using this method, gives the variation of K_I along the crack front, while the compliance method just gives an average stress intensity factor. By using both approaches a better understanding of the variation of K_I with the crack length can be determined, for the chevron-notched specimens.

Chapter III

Three-Dimensional Boundary Integral Equation Method

3.1. Introduction

Three dimensional elasticity does not enjoy the wealth of solutions that are available in two-dimensional elasticity. Solutions, for example, have been obtained for infinite and semi-infinite regions using the stress functions techniques, which satisfy the desired boundary conditions near the origin and have the properties that the stress and/or displacement vanish or remain bounded as the boundary at infinity is approached.

For finite three-dimensional problems analytical solutions have been used for simple geometries and loading conditions. However, for most engineering problems purely numerical methods such as finite difference and finite element are necessary. In these methods the whole continuum is discretized making the solution sensitive to the geometry of discretization.

Another method of analysis recently rediscovered by Rizzo in 1967 [20], the boundary integral equations method, offers an attractive alternative. The boundary integral method involves the transformation of the partial differential equations describing the behavior of the unknowns inside and on the

boundary of the domain to integral equations over the boundary, i.e. the integrals are functions of the boundary data only. Values at interior points if required can be calculated afterwards from the surface data. The system of equations resulting from discretization of the boundary integral equations may be smaller by an order of magnitude than that obtained by, for example, the finite element or finite difference methods. One drawback is that the resulting matrices are non-symmetric and fully-populated, whereas in finite element methods the matrices are symmetric and most of the time banded.

3.2. Mathematical Derivation

The most direct derivation of the boundary integral equations is based on a singular solution of the Navier equations. The Navier equations of equilibrium (in terms of displacements) for three-dimensional problems in elasticity (for brittle materials) are :

$$\nabla^2 u_i + \frac{1}{1-2\nu} \theta_{,i} = 0 \quad (3.1.a)$$

$$\theta = u_{j,j} \quad i,j = 1,2,3$$

where u_j are the displacements, ν is Poisson's ratio and the usual tensor notation is used, where a repeated subscript indicates summation over its range and a comma indicates partial differentiation. The Navier equations can be written in another form as :

$$u_{i,jj} + \frac{1}{1-2\nu} u_{k,ki} = 0 \quad (3.1.b)$$

A solution to these equations can be obtained by making use of Kelvin's singular solution due to a single unit concentrated force acting in the interior of an infinite body [13] (see Figure 5).

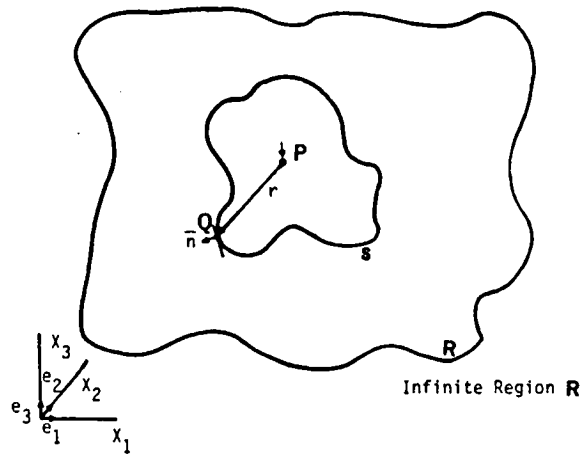


Figure 5. Point load in an infinite region

The displacement field at any point \$Q\$ at distance \$r\$ from the point where the force is applied is given by Ref. [15] :

$$u_j = \frac{1}{4\pi G} \left[\frac{1}{r} \right] \left\{ \frac{3-4\nu}{4(1-\nu)} \delta_{ij} + \frac{1}{4(1-\nu)} r_{,i} r_{,j} \right\} \cdot e_i \quad (3.2.a)$$

or

$$u_j = u_{ij} \cdot e_i \quad (3.2.b)$$

and

$$u_{ij} = \frac{1}{4\pi G} \left[\frac{1}{r} \right] \left\{ \frac{3-4\nu}{4(1-\nu)} \delta_{ij} + \frac{1}{4(1-\nu)} r_{,i} r_{,j} \right\}$$

where r is the distance between a field point Q with coordinates (x_i) and the point of load P with coordinates (X_p) ;

$$r = \left[(X_i - X_p) (X_i - X_p) \right]^{1/2} \quad (3.3)$$

and e_i is the component of the unit base vector in the i direction.

If we consider the field point Q to be on the boundary of a body cut out of the infinite region, then by making use of the solution for the displacement field u_j , the traction forces can be determined on this boundary by

$$t_j = \sigma_{ji} \cdot n_i \quad (3.4)$$

where n is the outward normal at the surface of the body.

Expressing the stress tensor in terms of displacements

$$\sigma_{ji} = \frac{2G\nu}{1-2\nu} \delta_{ji} u_{m,m} + G [u_{j,i} + u_{i,j}] \quad (3.5)$$

where G is the shear modulus, differentiating equations (3.2) and substituting in Equation (3.5), equation (3.4) becomes :

$$t_j = \frac{-(1-2\nu)}{8\pi(1-\nu)} \left[\frac{1}{r^2} \right] \left[\frac{dr}{dn} \left[\delta_{ij} + \frac{3}{(1-2\nu)} r_{,i} r_{,j} \right] - n_j r_{,i} + n_i r_{,j} \right] \cdot e_i \quad (3.6.a)$$

or

$$t_j = T_{ji} \cdot e_i \quad (3.6.b)$$

where

$$T_{ij} = \frac{-(1-2\nu)}{8\pi(1-\nu)} \left[\frac{1}{r^2} \right] \left[\frac{dr}{dn} \left[\delta_{ij} + \frac{3}{(1-2\nu)} r_{,i} r_{,j} \right] - n_j r_{,i} + n_i r_{,j} \right]$$

We now make use of Betti's reciprocal theorem [14] which states: If an elastic body is subjected to two systems of surface tractions t_j and t_j^* , then the work that would be done by the first system t_j in acting through the displacement u_j^* of the second system is equal to the work that would be done by the second system t_j^* acting through the displacement u_j of the first system, i.e.

$$\int_s t_j u_j^* ds = \int_s t_j^* u_j ds \quad (3.7)$$

where s is the boundary surface of the body, and ds is an element of surface area.

Suppose we now choose the second system of traction and displacement (t_j^* and u_j^*) to be the one produced by a single unit concentrated load, and the system u_j , t_j to correspond to

the solution we are seeking, then since we know the solution to the unit concentrated load (Kelvin solution), we can solve for any of the unknown traction and displacement (t_j, u_j) by substituting equations (3.6) and (3.2) for t_j^* and u_j^* respectively, and solving the integral equation (3.7). Because of the singular nature of U_{ij} and T_{ij} at $r = 0$, it is necessary to employ a limiting process as shown in Appendix A, resulting in the following equation, known as the boundary integral equations:

$$\int_S t_j U_{ij} ds = \int_S u_j T_{ij} ds - \delta_{ij} u_j \quad (3.8.a)$$

or in another form

$$C_{ij} u_j = \int_S U_{ij} t_j ds - \int_S T_{ij} u_j ds \quad (3.8.b)$$

where $C_{ij} = \delta_{ij}$ for interior points and $C_{ij} = \frac{\delta_{ij}}{2}$ for boundary points with smooth tangents. Equations (3.8) are also known as Somigliana's identity. For very simple geometries and boundary conditions Somigliana's identity is satisfactory for obtaining analytical solutions, but for complex bodies a numerical solution is necessary and is discussed in the next chapter.

Once the unknown traction and displacement are determined on the boundary, internal displacements and stresses can be calculated as functions of the boundary displacements and tractions. For internal displacement, equations (3.8) is used with $C_{ij} = \delta_{ij}$, however for internal stresses equations (3.8) is

differentiated and substituted in equation (3.5), to get [15]:

$$\sigma_{ij} = \int_S \{ v_{ijk} t_k - T_{ijk} u_k \} ds \quad (3.9)$$

where

$$v_{ijk} = \frac{1}{8\pi(1-\nu)r^2} \left\{ (1-2\nu)(\delta_{ik}r_{,j} + \delta_{jk}r_{,i}) + 3r_{,i}r_{,j}r_{,k} - \delta_{ij}r_{,k}(1-2\nu) \right\}$$

$$T_{ijk} = \frac{G}{8\pi(1-\nu)r^3} \left\{ 6 \frac{dr}{dn} [\nu \delta_{ik}r_{,j} + \nu \delta_{jk}r_{,i} + (1-2\nu)\delta_{ij}r_{,k} - 5r_{,i}r_{,j}r_{,k}] + 6\nu r_{,k}r_{,i}n_j + 6\nu r_{,j}r_{,k}n_i + 6(1-2\nu)r_{,i}r_{,j}n_k - 2(1-4\nu)\delta_{ij}n_k + 2\delta_{ik}n_j + 2\delta_{jk}n_i \right\}$$

Thus, the displacements and stresses at any interior point can be obtained by integrating numerically over the boundary equations (3.8) and (3.9) respectively with $c_{ij} = \delta_{ij}$, in the absence of body forces.

CHAPTER IV

NUMERICAL PROCEDURE

4.1. Reduction of the Integral Equation to a set of Simultaneous Equations

The first step in solving the boundary integral equations is to reduce them to a set of linear simultaneous equations. The boundary of a body to be analyzed is divided into N surface segments. Those segments can be rectangles or triangles as seen in Figure 6. Eq. 3.8 can then be rewritten as:

$$C_{ij} u_j = \sum_{n=1}^N \int_{s_n} U_{ij} t_j d s_n - \sum_{n=1}^N \int_{s_n} T_{ij} u_j d s_n \quad (4.1)$$

As an approximation the traction, t_j and displacement, u_j are assumed constant over each surface segment, and concentrated at the centerpoint of that segment. Equation (4.1) can be written as:

$$C_{ij} u_j = \sum_{n=1}^N t_j \int_{s_n} U_{ij} d s_n - \sum_{n=1}^N u_j \int_{s_n} T_{ij} d s_n \quad (4.2)$$

The expression (4.2) represents a set of $3N$ equations which can be written in matrix form as:

$$\left[C_{in} + \int_{s_n} T_{in} d s_n \right] \left\{ u_j^n \right\} = \left[\int_{s_n} U_{in} d s_n \right] \left\{ t_j^n \right\} \quad (4.3.a)$$

where $j = 1, 3 \dots i, n = 1, N$

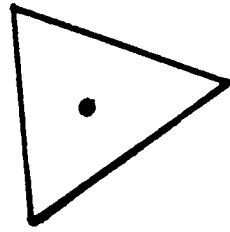
or in general form

$$[A] \{u\} = [B] \{t\} \quad (4.3.b)$$

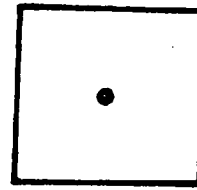
For the case of a traction problem where the t 's are known, or the case of a displacement problem where the u 's are known, equation (4.3) reduces to the form

$$[A] \{X\} = \{C\} \quad (4.4)$$

Equations (4.4) represents a set of $3N$ linear algebraic equations which are to be solved by Gauss Elimination method. In case of mixed boundary value problem, where some values of both t and u are specified, it is necessary to interchange the columns of matrices A and B (in Eq. 4.3), that all the unknown quantities are contained in the column vector u and the known values are contained in t , before reducing the equation to the form of Eq. (4.4).



Constant Triangular
Element



Constant Rectangle
Element

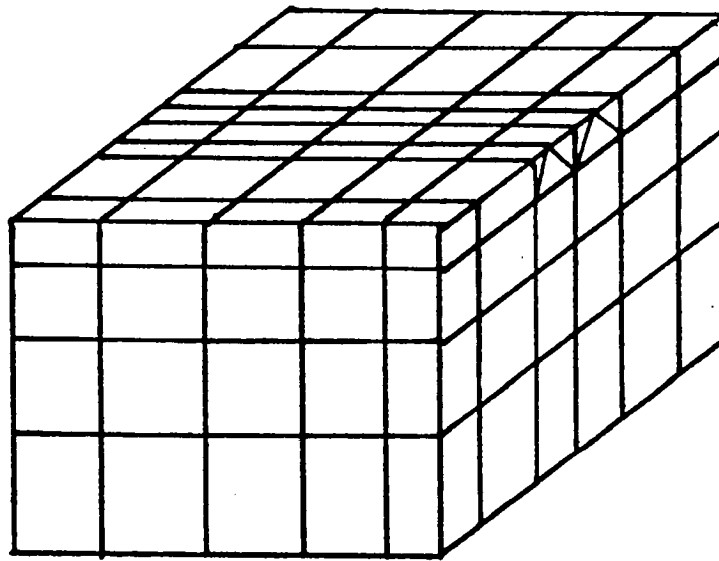


Figure 6. Typical surface mesh for constant segment

The assumption of constant values of t and u is a good approximation for simple problems. However when a stress gradient exists, this method needs a very large number of surface segments to converge.

As an improvement, the traction and displacement are assumed to vary linearly over each surface segment. Values of tractions and displacements are assigned to nodes located at the corners of the triangular or rectangular segments rather than at their centerpoints (See Figure 7). A review of the linear variation used, and the integration methods implemented in the computer program written are shown in appendix B.

By placing the nodes at the corners of the segments two difficulties become apparent:

1) The possibility exists for nodes to be placed at sharp edges of the body rather than at flat surfaces. While C_{ij} (in Eq. 4.1) is equal to $1/2 \delta_{ij}$ for flat surfaces (see chap. 3 for explanation of δ_{ij} and C_{ij} terms), C_{ij} for nodes at edges must be computed, using a limiting process derived as explained in Ref. [18].

$$C_{ij}(P,Q) = -\sum_{n=1}^N \int_{s_n} T_{ij}(P,Q) ds_n \quad \text{for } P \neq Q \quad (4.5)$$

In the computer program, all C_{ij} terms are computed using Eq.(4.5) . The value for C_{ij} on flat surfaces was computed and

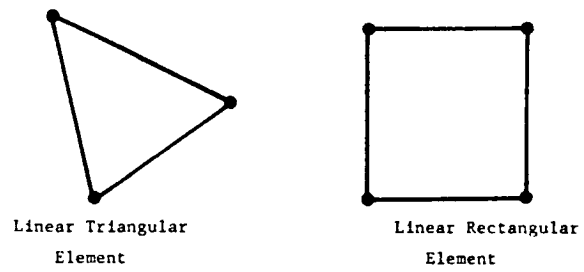


Figure 7. Linear segments

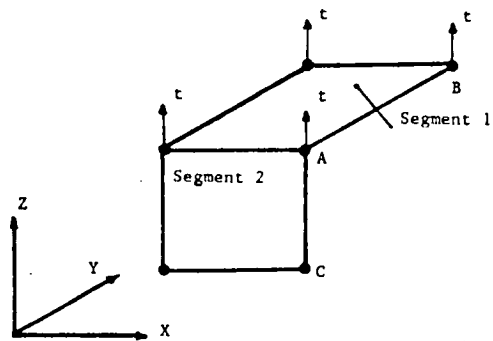


Figure 8 . Intersection of two segments that lie in different planes

it was found to be exactly equal to $1/2 \delta_{ij}$ as predicted by the analytical formulation.

2) Placing nodes at corners of segments assures the continuity of displacements and tractions. However, in modelling real problems a step change in traction may exist. To assure discontinuity of applied tractions, the input values of traction are associated with the segment they act on instead of the nodes. As an example, consider two adjacent segments which lie in two different planes (see Figure 8). Segment 1 is under uniform tension t while segment 2 is traction free. If the traction is associated with node A directly, an extra shearing traction exists in segment 2 varying from zero at node C to t at node A. By assigning the traction to a node of a specific segment, in this example to node A of segment 1, the problem of adding extra traction is avoided. Alternatively, one can place two distinct nodes between segments 1 and 2, but this method is not implemented here.

Another problem due to the discontinuity of traction occurs at crack fronts. To solve this problem the crack front is left free of surface segments (see Figure 9). This method causes oscillation of the traction distribution ahead of the crack front: This oscillation is demonstrated in the next section. To avoid these oscillations, two special segments are used near crack fronts. In the first case, the surface segment adjacent to

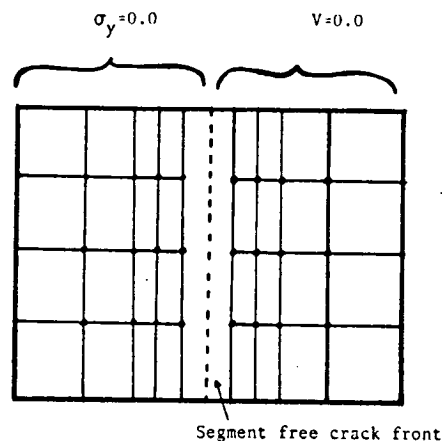


Figure 9. Segment free crack front

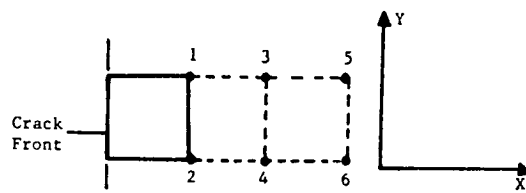
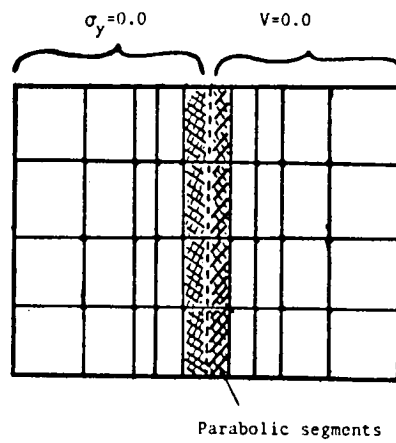


Figure 10. Parabolic segment for discontinuity regions near crack fronts

the discontinuity is assumed free of nodes. The traction and displacement in this surface segment is assumed to be a parabolic (the next highest order of magnitude after linear variation) function of the tractions and displacements of the six nodes behind it (see Figure 10). The variation of the traction, and displacement over the node free segment has the form.

$$t = S_1 t^1 + S_2 t^2 + S_3 t^3 + S_4 t^4 + S_5 t^5 + S_6 t^6$$

$$u = S_1 u^1 + S_2 u^2 + S_3 u^3 + S_4 u^4 + S_5 u^5 + S_6 u^6$$

$$S_1 = \frac{(x - x_3)(x - x_5)(y - y_2)}{(x_1 - x_3)(x_1 - x_5)(y_1 - y_2)} \quad ; \quad S_2 = \dots\dots\dots$$

Where x, y are the in-plane coordinates of the nodes. When $x = x_1$ and $y = y_1$, $S_1 = 1$ and all the other S 'n are equal to zero. This variation is based on Lagrange's interpolation formula.

When the number of nodes around the discontinuity is smaller than six, a simplified constant segment is used. This simplified constant segment is the same as a regular constant triangular segment, except that the node is positioned at one of the corners rather than at its centerpoint (see Figure 11).

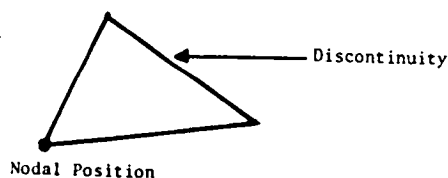


Figure 11. Special constant segment

While the linear variation is more complex than the constant model, little extra effort is required to assemble the matrix in the form of equation (4.4). The resulting system was then solved by the Gauss Elimination Method on the CRAY-1 system at NASA Lewis Research Center.

To check the computer program, the Single-Edge-Cracked-Tension specimen (SECT), shown in Figure 12, is analyzed, and the results of the stress intensity factors are compared with two other methods (the method of line and finite element) as shown in the next section.

4.2 Results For The Single-Edge-Cracked-Tension Specimen

The computer program of the Boundary Integral Equations (BIE), is first applied to a single-edge-cracked specimen in tensile loading. The SECT specimen has dimensions, $W = 2.0$, $B = 3.0$, $H = 1.75$, $a = 1.0$, and Poisson's ratio equal to 0.333, where a , B , W , and $2H$, are the specimen's crack length, thickness, width, and height, respectively (see Figure 12). The same SECT specimen has also been analyzed by the Finite Element Methods (FEM) in Ref. [16], and by the Method of Lines (MOL) in Ref. [17]. The effect of the discontinuity segments is also studied below.

Two computer runs of identical number of nodes (304), are used in this study. The difference between the two meshes is that mesh A contains discontinuity segments while B uses segment free crack front. A plot of the normalized stress distribution at the center of the specimen is shown for both meshes (Figure 13). Also shown is the Finite Element stress distribution. From the results, two observations can be made: 1) The stress distribution for mesh B oscillates sharply near the crack tip, 2) the stress distribution for mesh A agrees with the FEM results. The effect of the discontinuity segments is not apparent in the plot of the displacement distribution (Figure 14), and the results of the displacement seem in good agreement with FEM. The difference between the displacements of meshes A and B is accentuated in determining the stress intensity factor from Eq. (2.16).

In Figure 15, a plot of the displacements at the center of the SECT specimen Divided by the square root of the distance r from the crack front, is shown for both meshes. The solution of mesh B (with segment free crack front) diverges as r goes to zero. The solution for mesh A (with special segments at the crack front) is almost a linear function of r . This behavior of mesh A at the center of the specimen is true throughout the thickness as seen in Figure 16. The stress intensity factor (SIF) is then determined through the thickness of mesh A as described in section 2.5 using the displacements. A plane strain

condition is assumed throughout the thickness of the specimen, except at the surface where a plane stress is assumed. Correspondingly α in Eq. (2.16) is equal to 3.556 for plane strain and 4.0 for plane stress. Figure 17 shows the variation through the thickness of the dimensionless stress intensity factor ($\frac{k}{\sigma \sqrt{\pi a}}$), obtained by the BIE method with discontinuity segments as well as the FEM and the MOL. There is a -2.5 percent difference between BIE and FEM at the center and +4.0 % at the outer surface of the specimen. The difference between BIE and MOL is only -1.4 % as shown in Table 1.

Table 1--Normalized stress intensity factor for Sect

specimen, $W = a = 1.0$, $B = 3.0$, $H = 1.75$, $U = 0.333$.

$\frac{z}{B}$	BIE	FEM [16]	MOL [17]
0.000	2.72	2.79	2.76
0.266	2.70	2.76	2.78
0.483	2.47	2.43	2.47
0.500	2.24	2.15	2.38

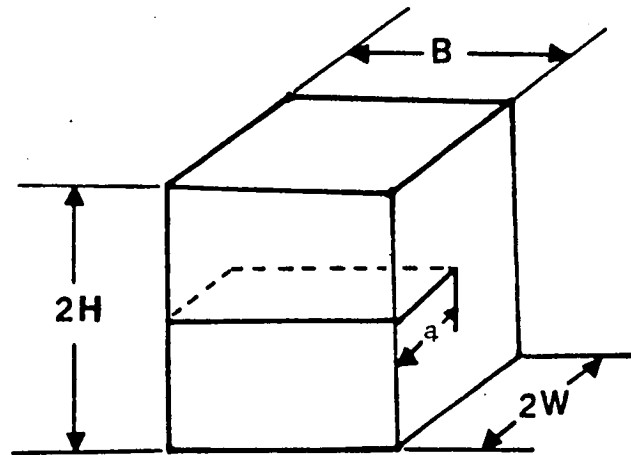


Figure 12. Single-Edge-Cracked-tension specimen

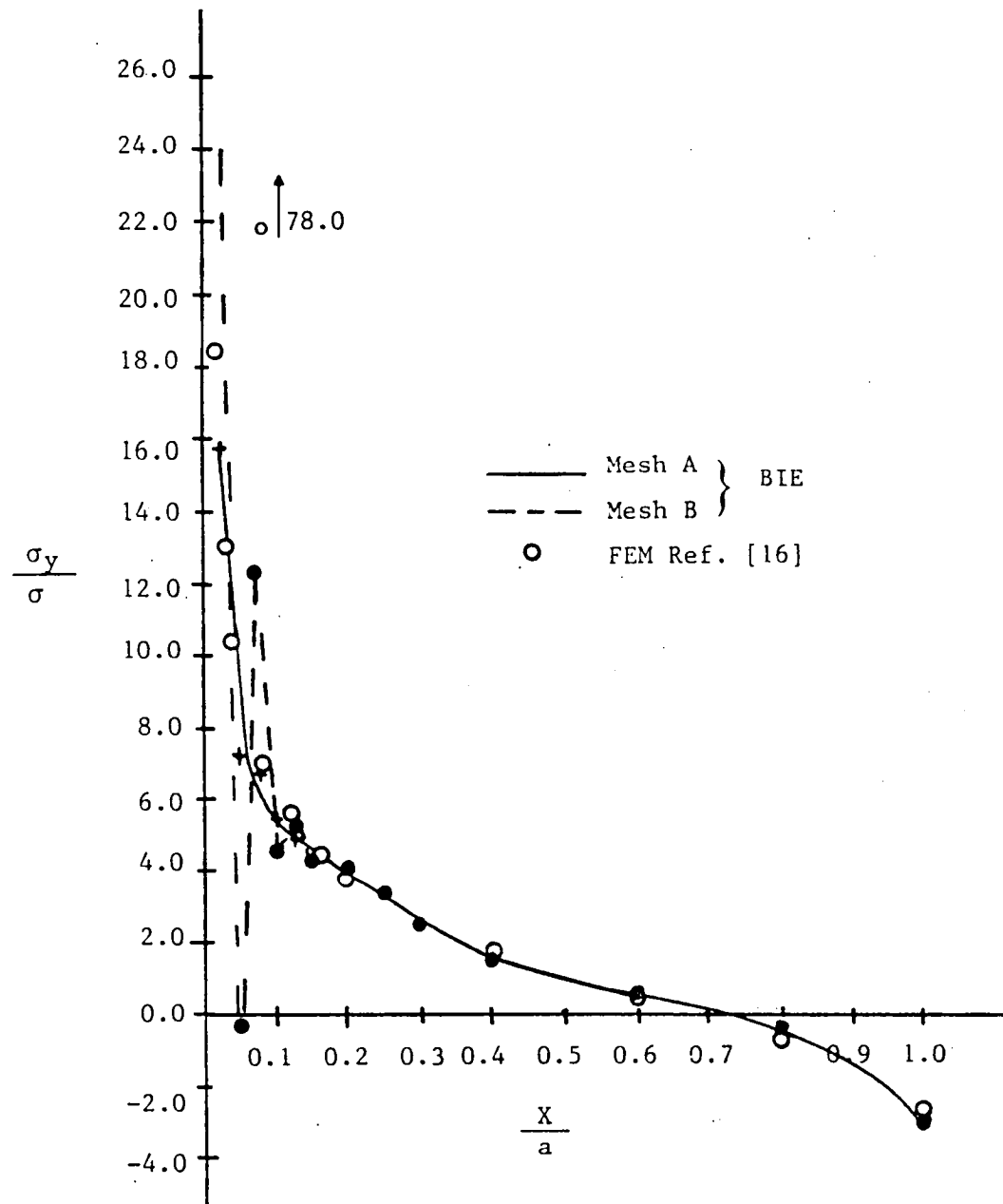


Figure 13. Stress distribution at the centerline of the SECT specimen

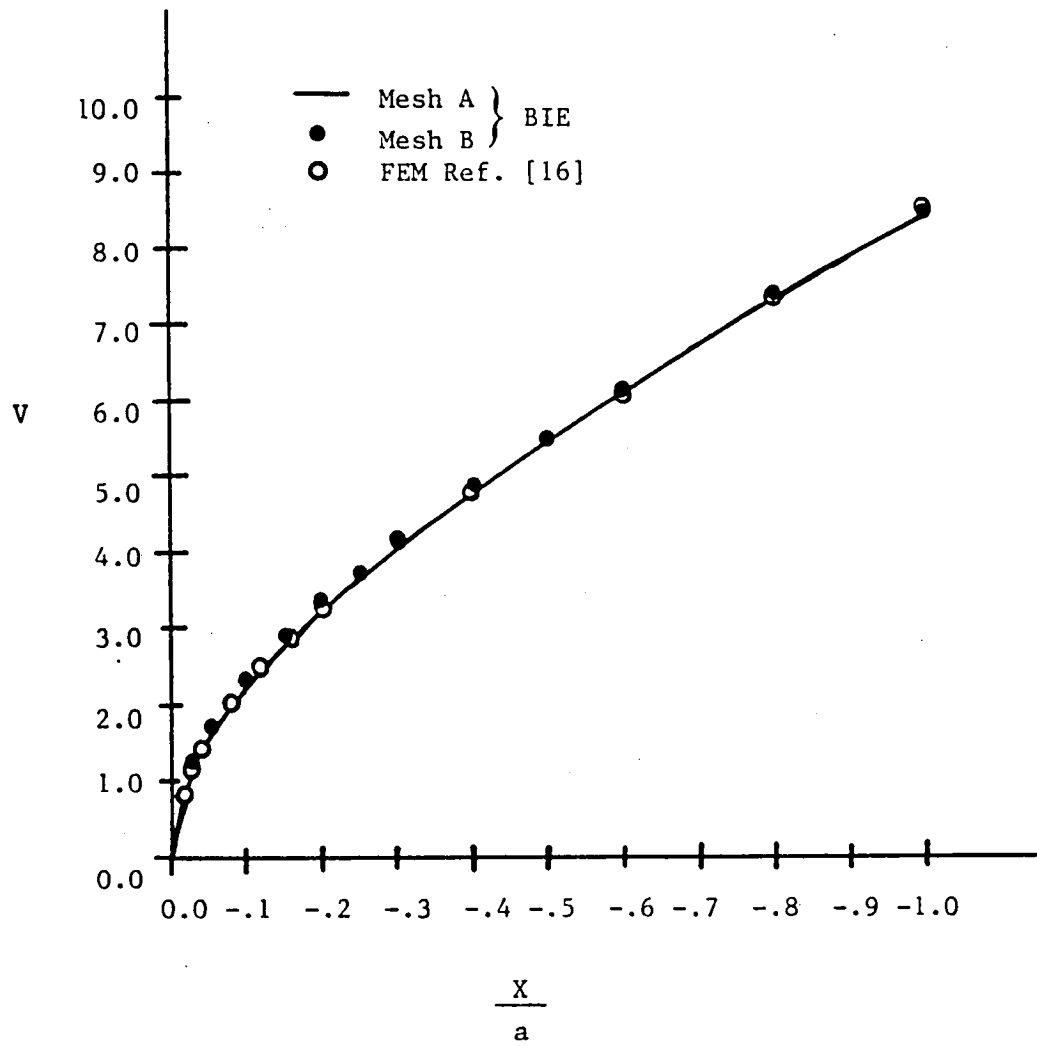


Figure 14. Displacement distribution at the centerline of the SECT specimen

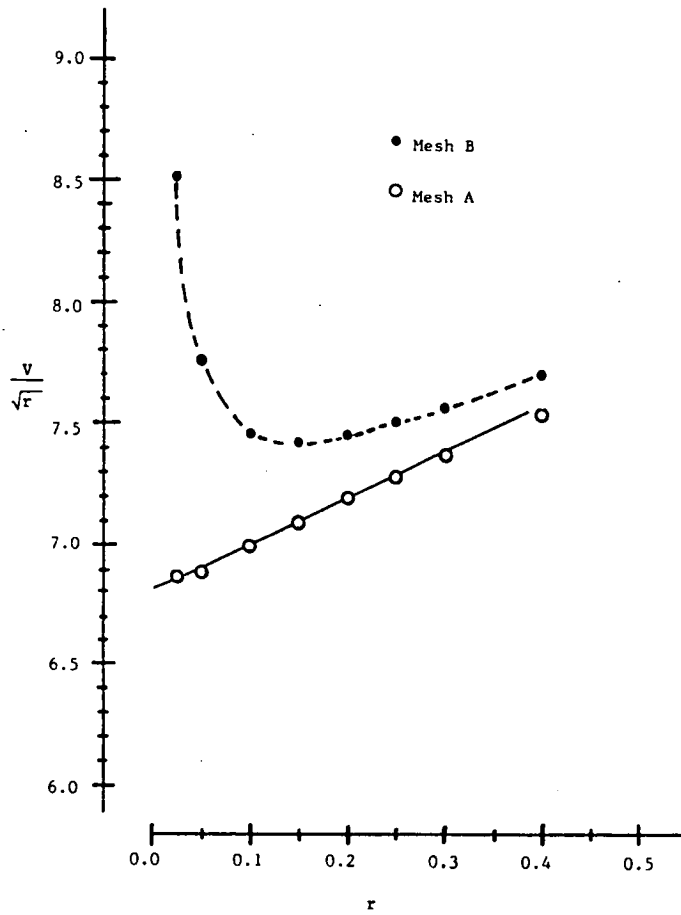


Figure 15. V/\sqrt{r} versus r for the two meshes of the SECT specimen

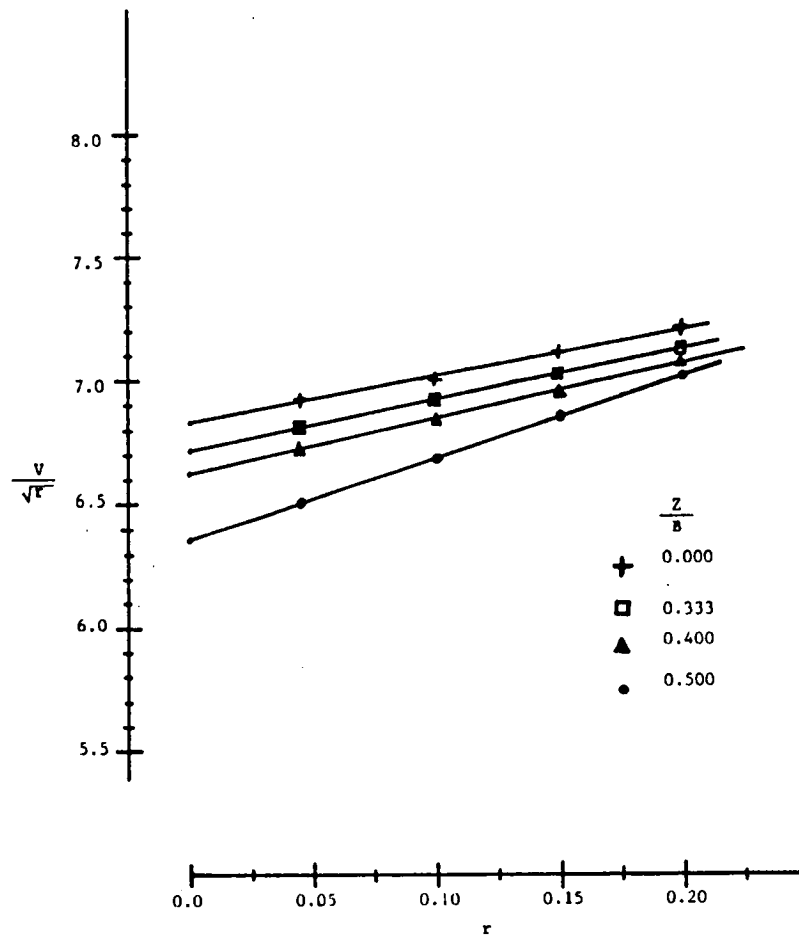


Figure 16. Variation of V/\sqrt{r} along the crack front for SECT

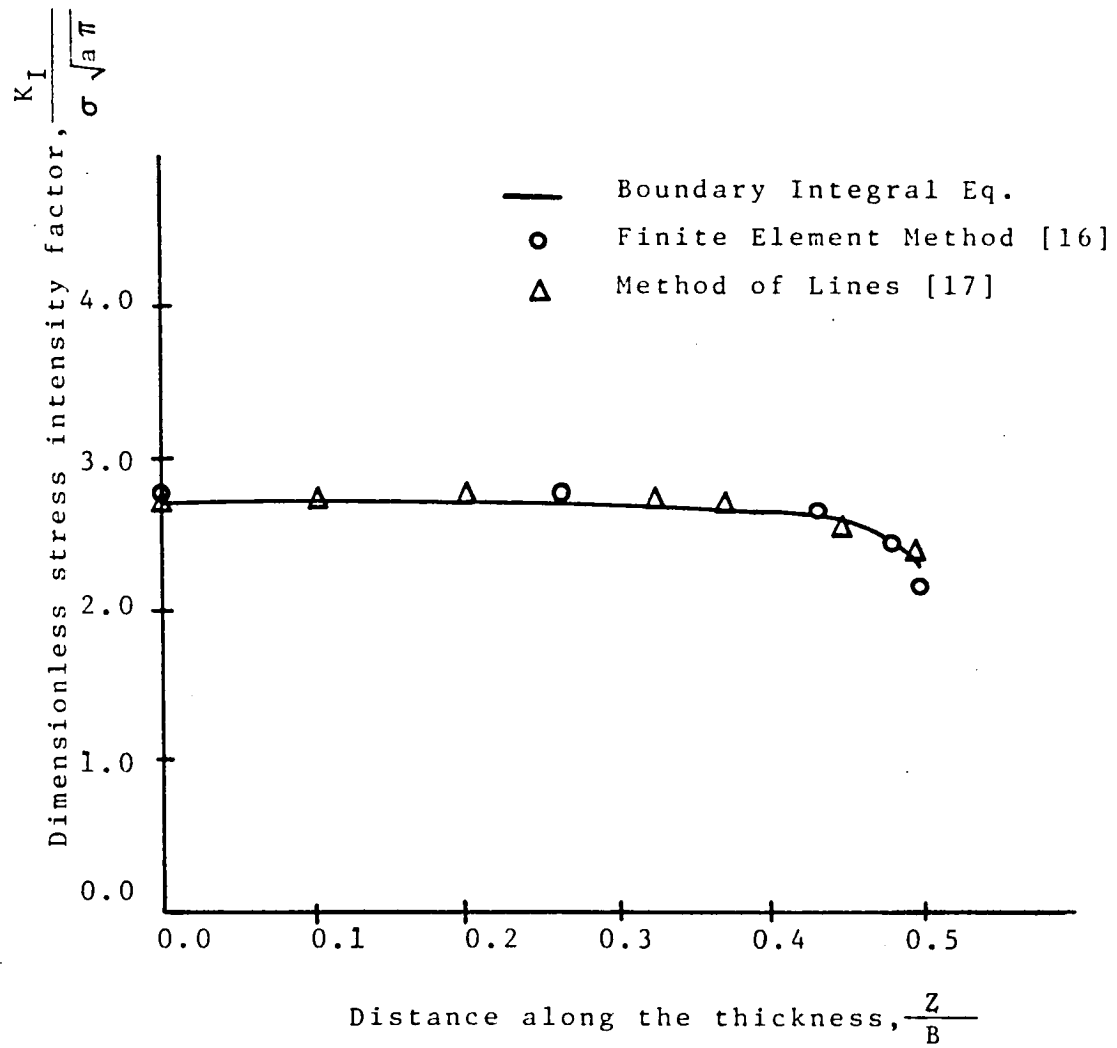


Figure 17. Normalized stress intensity factor for the SECT specimen

The SIF decreases approximately by 18 % in going from the center to the surface of the specimen for BIE, compared with only 15 % for MOL and 23 % for FEM. The difference of less than 5 % for the three methods can be considered a good agreement, for a three dimensional fracture mechanics problem.

4.3 Discretization of the Chevron-Notched Specimens.

Having verified the accuracy of the equations and the computer program on the SECT specimen, a convergence study on the Chevron-Notched short-bar specimen is performed in this section. The basic dimensions of the specimen are:

$$B = 1.0, W = a_1 = 2.0, a_0 = 0.4, 2H = 1.0, U = 0.333,$$

$$W + x' = 2.10$$

where x' is the distance between the loading line and the end of the specimen as seen in Figure 18. x' is equal to $0.1B$. In terms of the dimensionless quantities $\alpha_1 = a_1/W$, the values of α_0 and α_1 are 0.2 and 1.0 respectively. A square grip groove is also modelled having the dimensions recommended by ASTM E24.01.05 task group. The total height of the groove is $0.35B$ and its depth is $0.15B$. The only discrepancy with the recommendation is the absence of the finite width slot cut into the actual specimens to form the chevron-notch.

The usual loading of the chevron-notched specimens is with a knife edged fixture [6]. The type of loading applied in this analytical work is a uniform traction in the Z-direction and a

triangular variation in the X-direction, as shown in Figure 19.

The modulus of elasticity (E) used is equal to 1.0. This normalization of E is needed so that the coefficient of tractions and displacements will be of the same order of magnitude. This is of importance for mixed boundary value problems where the coefficient of matrices A and B (in Eq. 4.3) are interchanged to form a set of linear algebraic equations with all the unknowns on one side and the knowns on the other. If the coefficients of matrix A in Eq. (4.4) are not of the same order of magnitude, large truncation errors are induced in using Gauss Elimination method.

For the convergence study three meshes having different number of nodes are used. Mesh 1 shown in Figure 20 has 61 nodes and 72 boundary segments. Mesh 2 is basically formed by dividing every surface segment in mesh 1 into approximately four. Mesh 2 has 221 nodes and 237 boundary segments, and is shown in Figure 21. Finally, mesh 3 has 370 nodes and 420 boundary segments. Mesh 3 is shown in Figure 22. All meshes have discontinuity segments at the crack front, and linear segments everywhere else. Mesh 1 has one segment along the crack front, while mesh 2 has two segments and finally, mesh 3 has four.

Calculations were performed for nine different values of crack front positions ranging from $\alpha = 0.35$ to 0.75, on the three meshes described above. Figure 23 shows the dimensionless opening displacement EVB/P (see chapter 2) for the three meshes

(At $Y = 0.175$, $Z = 0$, $X = -a/W$) as function of α . For α less than 0.5, values of EVB/P are converging from below while for α greater than 0.5 the convergence is from above. Figure 24 represents the variation of the normalized displacement for $\alpha = 0.4$ as function of the number of nodes. Also shown is the unpublished experimentally measured values obtained from J.L. Shannon, NASA Lewis Research Center. This curve shows that an asymptotic value is not yet reached. Even if this analytical curve is extrapolated it cannot reach the experimental value: This is partly due to the difference in the finite slot size, making the analytical model stiffer than the experimental. Proving this using a mesh with node numbers larger than 370 is practically impossible without making use of external storage. Instead, a new mesh was generated using the number of nodes as mesh 3 (370 nodes), but with different arrangement of the boundary segments. As seen in Figure 25, the boundary segments of mesh 4 are increased in the plane of the crack and decreased everywhere else. This mesh is the same as in Ref.[10]. The opening displacement of mesh 4 is shown to be 10% less than mesh 3. A complete plot of the normalized opening displacement for different values of α is shown in Figure 26 for meshes 3 and 4. Also shown are the unpublished experimental results from J.L. Shannon, NASA Lewis Research Center. Two observations can be made 1) mesh 4 is stiffer than mesh 3 and 2) mesh 3 is consistently lower by 4% than the measured values. The crack mouth opening

Table 2--Crack Mouth Opening Displacement for Different Meshes.

a/W	Mesh 1	Mesh 2	Mesh 3	Mesh 4
	<u>61</u>	<u>221</u>	<u>370</u>	<u>370</u>
0.35	79.51	84.28	89.92	----
0.40	102.60	107.20	110.04	98.96
0.45	131.75	134.90	136.21	122.80
0.50	167.44	168.34	164.31	150.30
0.55	210.20	208.37	200.30	182.90
0.60	261.25	256.81	236.96	218.90
0.65	323.22	316.83	285.89	----
0.70	404.13	395.47	346.38	335.80
CPU TIME	18.0sec	214.0sec	655.0sec	780.0sec

displacements for all meshes are summarized in Table 2 as function of a/W , also shown is the running time in seconds (CPU) required for each mesh on the CRAY-1 computer.

Figure 27 shows typical curves for the crack opening distribution along the centerline of the short-bar specimen for different mesh sizes for $\alpha = 0.5$.

Using the results shown in Figure 26, the stress intensity factor K_I was computed from relation (2.13), a plane stress condition is assumed. As a first approximation the slope of the compliance curve was obtained by fitting every three points to a second degree polynomial in terms of α , since it gives better results for the derivative than the linear variation.

$$C^* = \frac{EVB}{P} = B1 + B2 \alpha + B3 \alpha^2$$

then, $\frac{dC^*}{d\alpha}$ at the mid point is

$$\frac{dC^*}{d\alpha} = B2 + B3 \alpha$$

The results are plotted in Figure 28 for the four meshes, together with the unpublished experimental values from J.L. Shannon, NASA Lewis Research Center. Every mesh shows a minimum, but the position of the minimum point varies from one mesh to another. From the results it seems that the stress intensity factor is converging from above. Meshes 3 and 4 are in good

agreement only for large values of α , but for smaller values mesh 4 gives lower results than mesh 3.

A final check on convergence is applied to the variation of the stress intensity factor along the crack front. The stress intensity factor is determined from Eq. (2.16) assuming plane strain conditions all through the crack front. A plot of the displacement divided by \sqrt{r} is shown in Figure 29 for $\alpha = 0.5$. As Z approaches the intersection of the crack front with the chevron-notch, V/\sqrt{r} diverges. This divergence is due to the inadequacy of modelling the intersection of the crack front with the chevron-notch. So only the points greater than 0.1 are used in the stress intensity factor calculations. Using this assumption the normalized stress intensity factor, Y^* , was evaluated along the crack front. Y^* along the crack front is shown in Figure 30 for meshes 1, 2 and 3, with $\alpha = 0.5$. A plot of Y^* at the center of the specimen ($Z = 0$) for $\alpha = 0.5$ is shown as a function of the number of nodes (Figure 31). It is seen that in going from mesh 2 to mesh 3 a 40% increase in nodes caused only a 6% decrease in the stress intensity factor. Figure 31 shows that an extrapolation of the curve would produce a decrease of less than 2% of the Y^* . Therefore, it is decided, given the limited memory space available on the computer, that mesh 3 would be the model discretization for all the other geometries including the short-rod specimens.

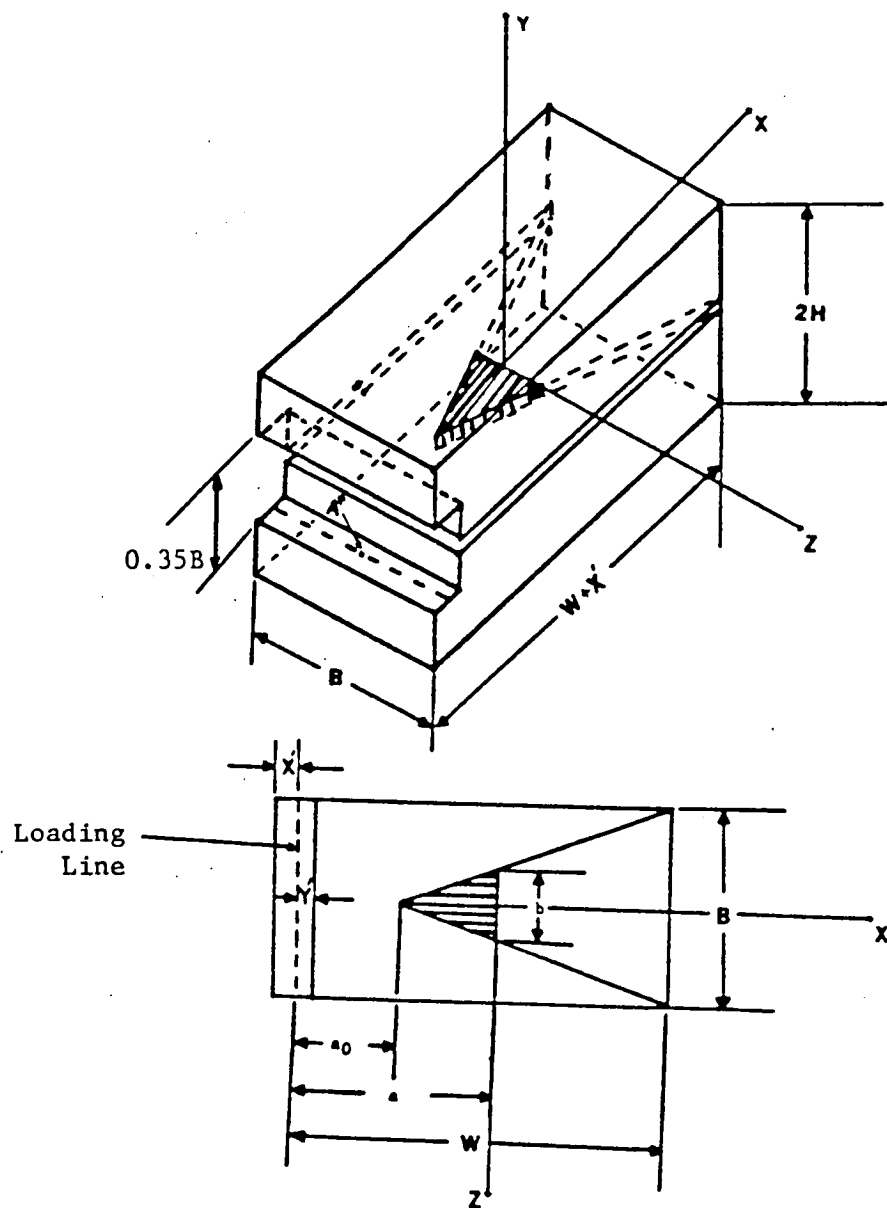


Figure 18. Chevron-notched bar specimen

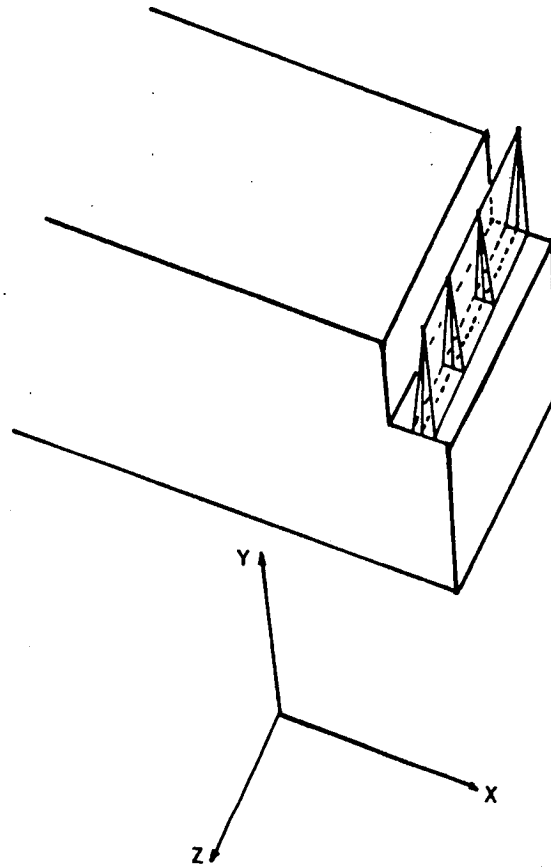


Figure 19. Loading condition for the chevron notched specimens

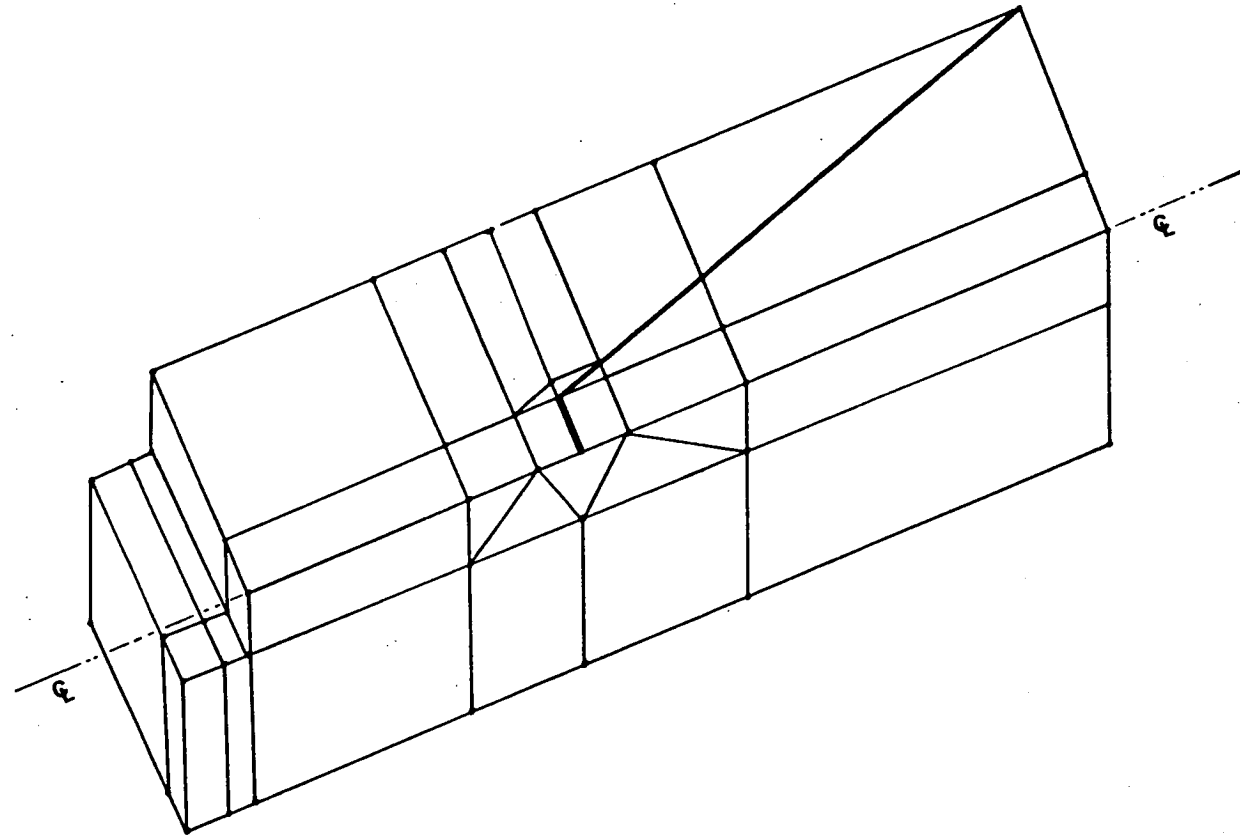


Figure 20. Mesh 1 with 61 nodes for $a/W = 0.4$

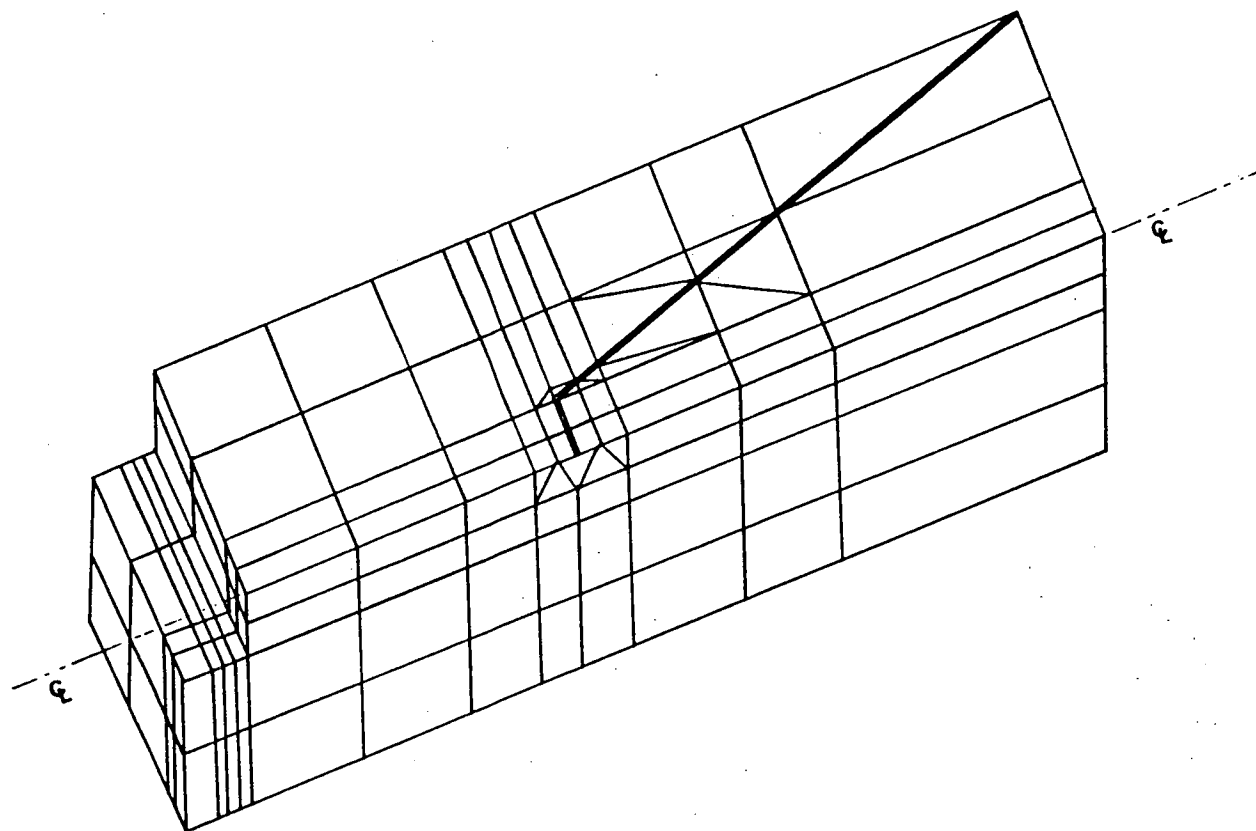


Figure 21. Mesh 2 with 221 nodes for $a/W = 0.4$

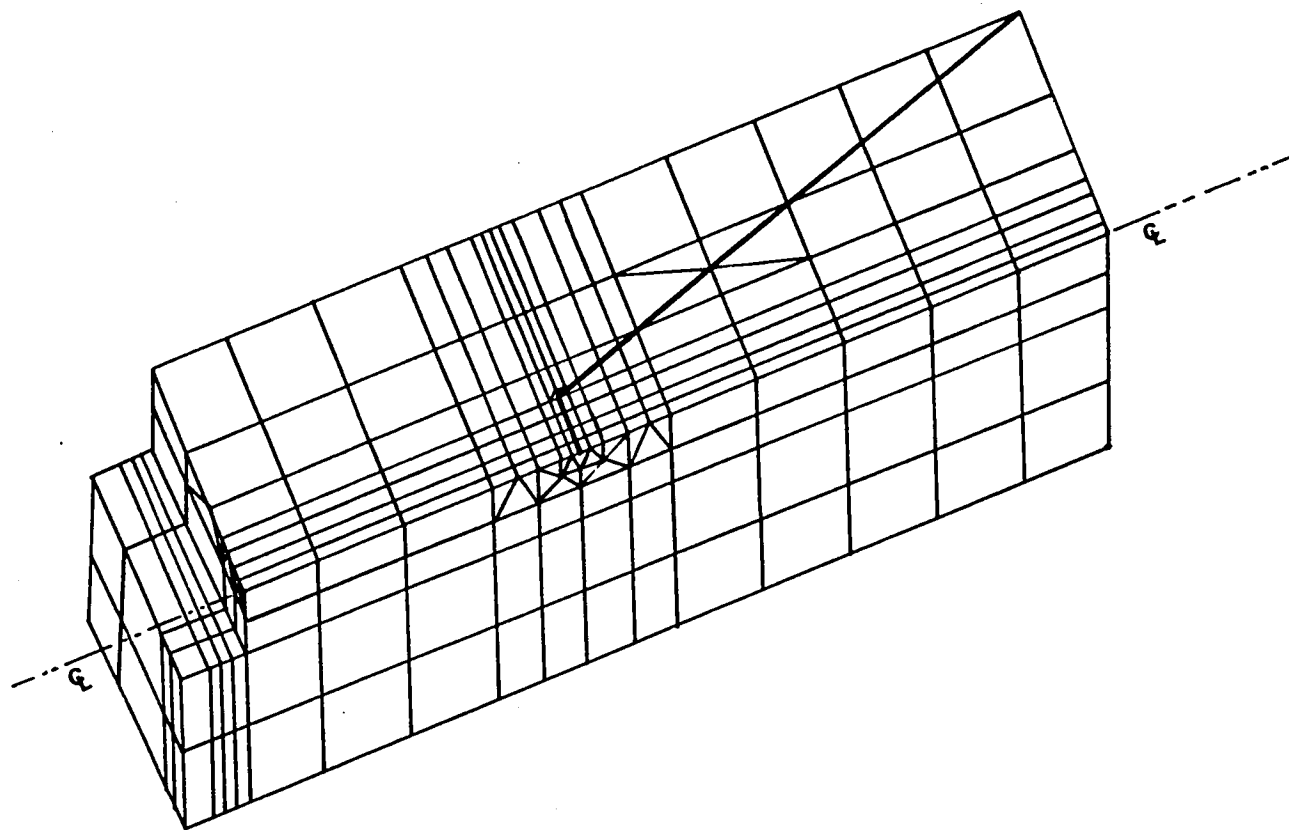


Figure 22. Mesh 3 with 370 nodes for $a/W = 0.4$

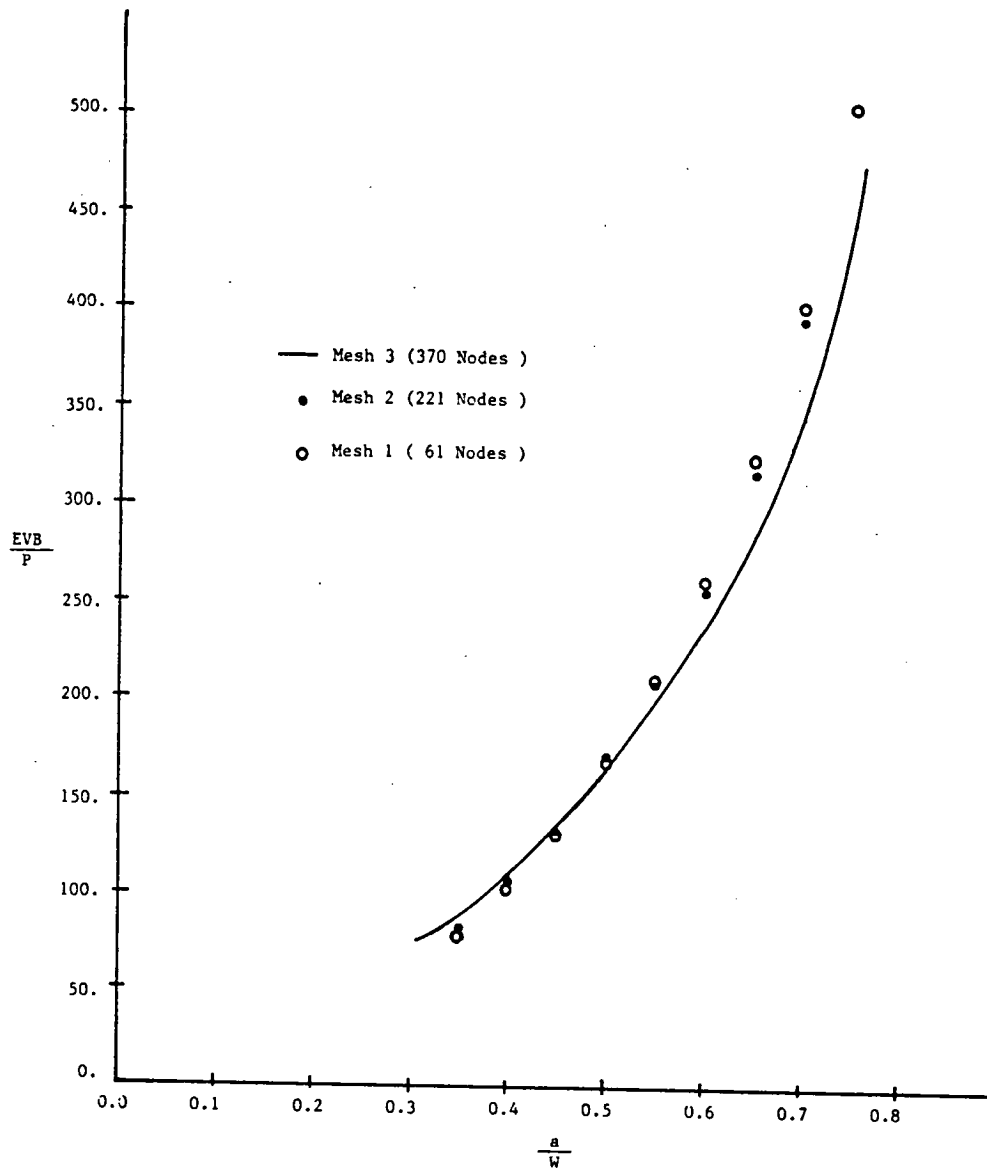


Figure 23. Crack opening displacement as function of a/W

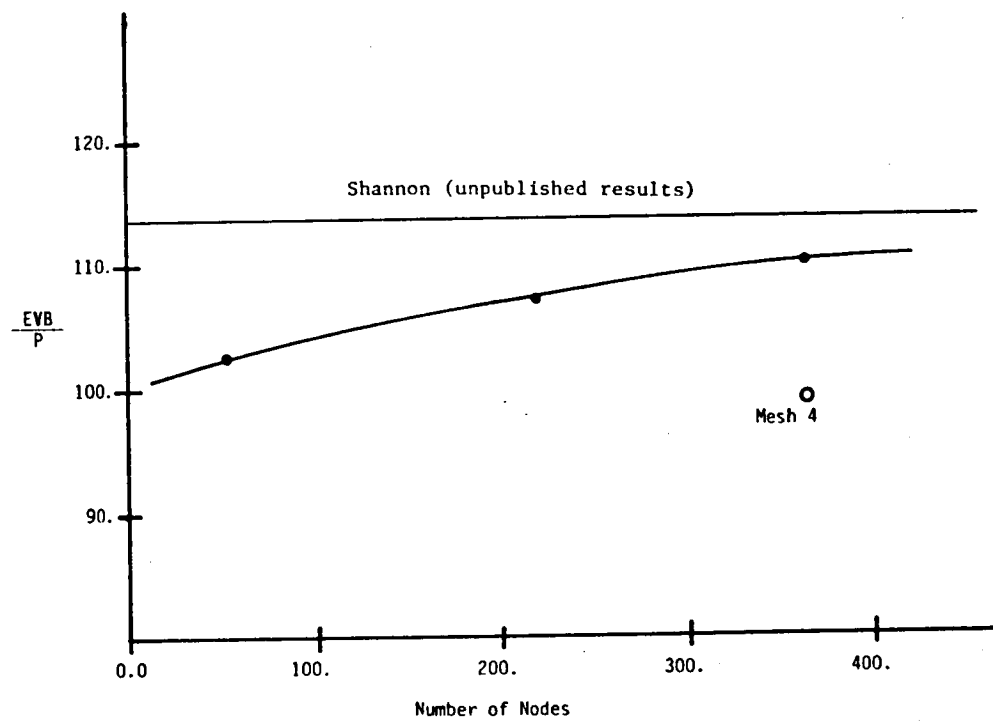


Figure 24. Crack opening displacement as function of the number of nodes for $a/W = 0.4$

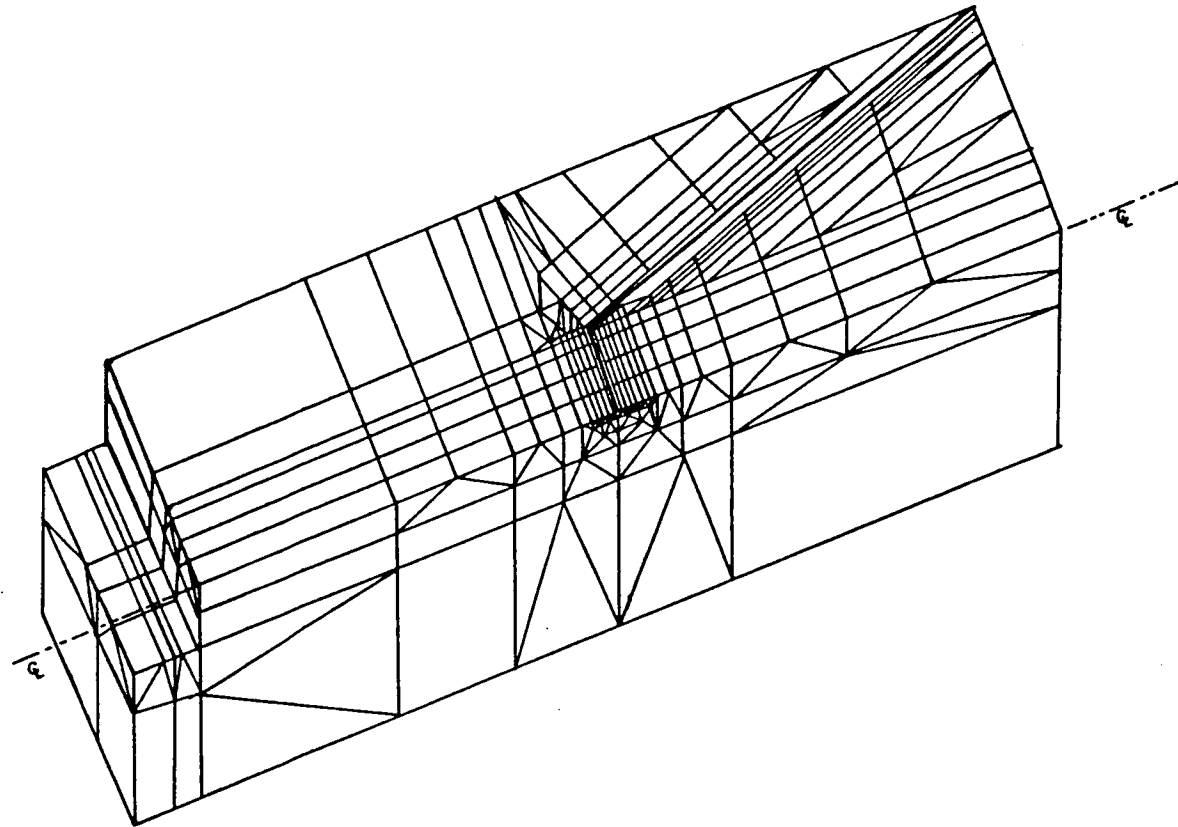


Figure 25. Mesh 4 with 370 nodes for $a/W = 0.5$

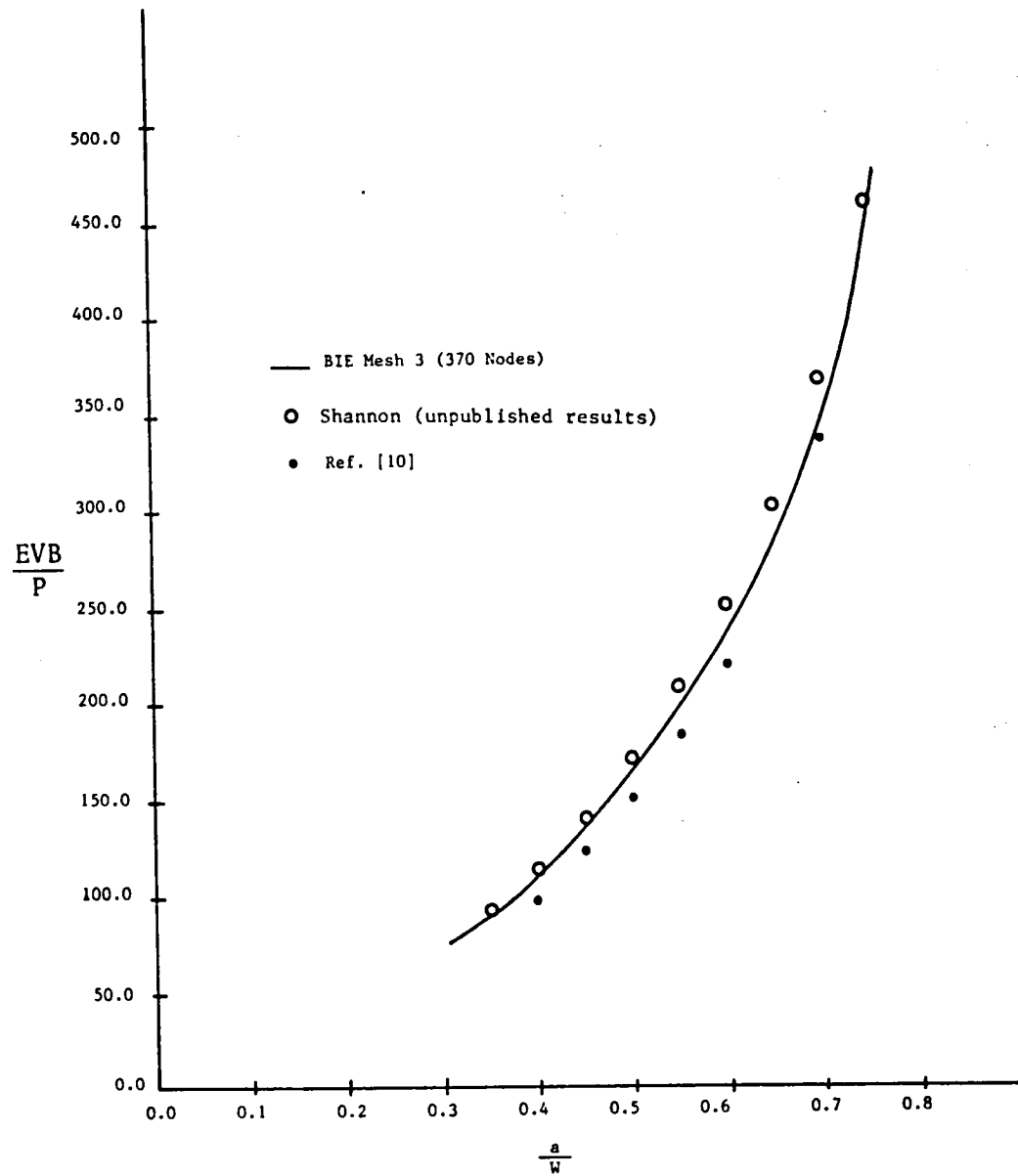


Figure 26. Normalized crack opening displacement as function of a/W

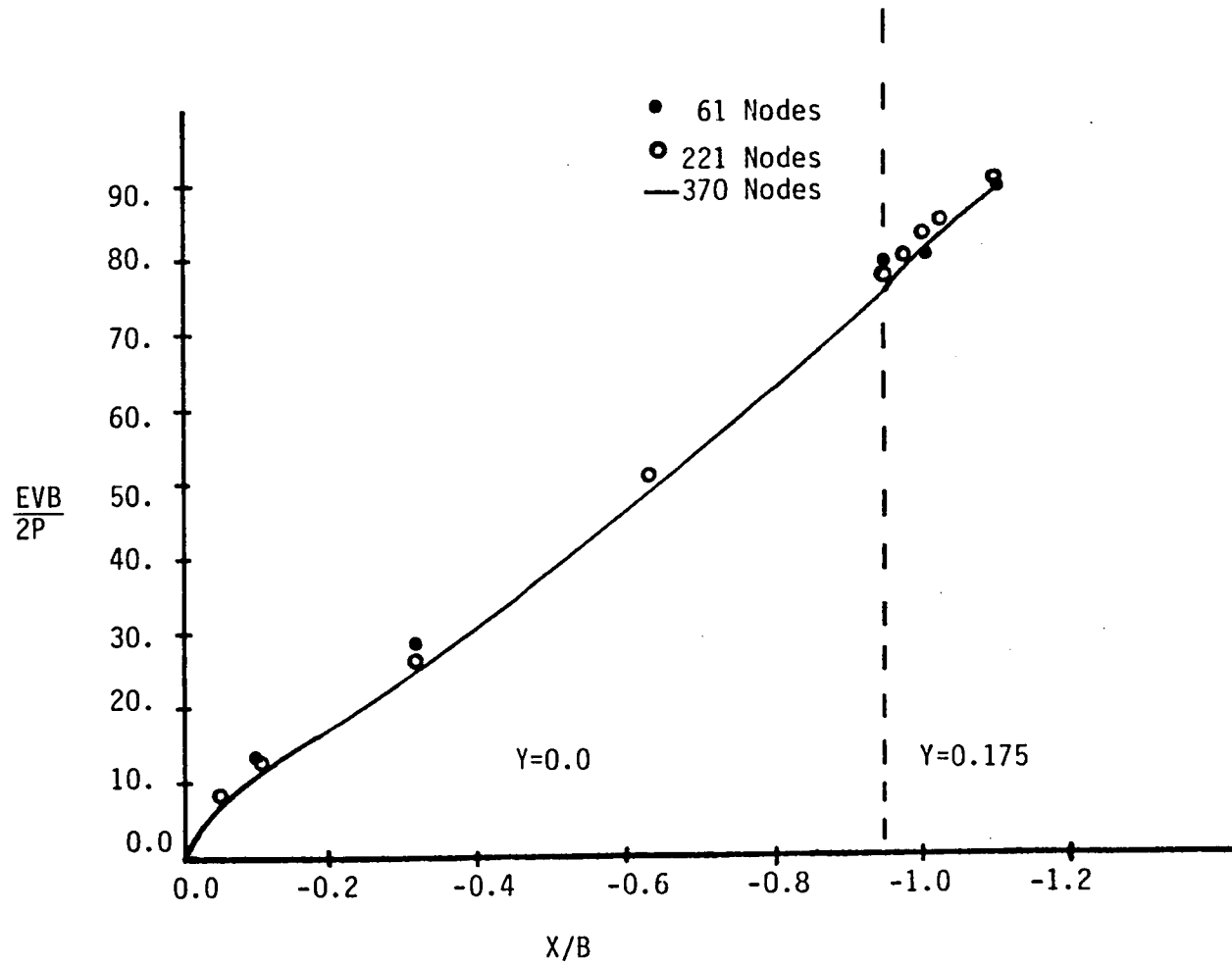


Figure 27. Normalized displacement distribution at the centerline of the short-bar specimen for $a/W = 0.5$

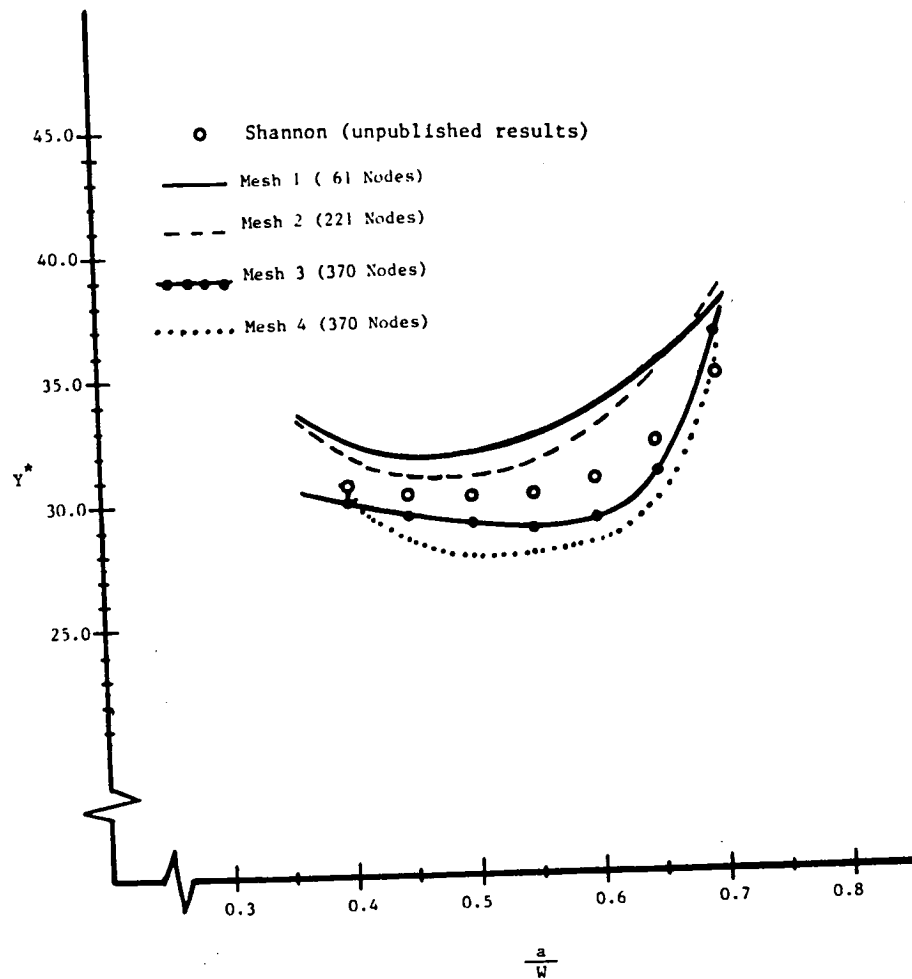


Figure 28. Normalized stress intensity factor as function of a/w (from compliance)

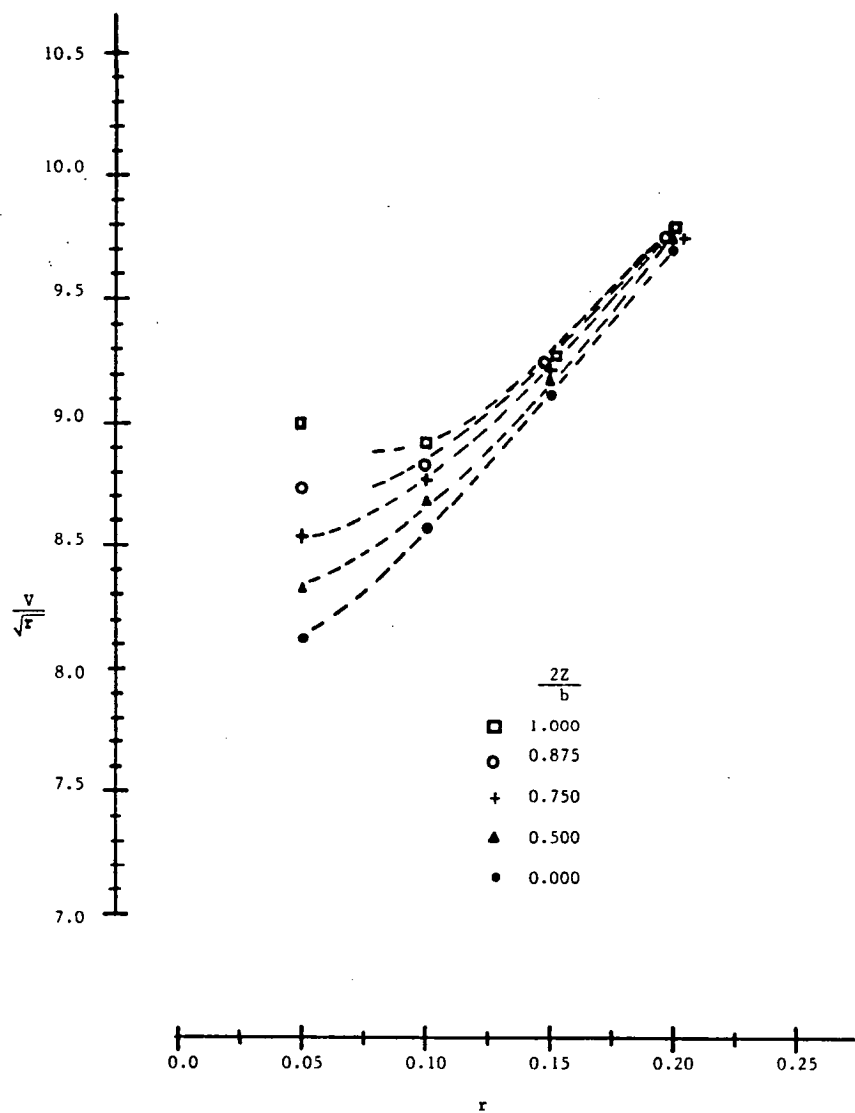


Figure 29. Variation of V/\sqrt{r} for the chevron notch bar specimen for $a/W = 0.5$

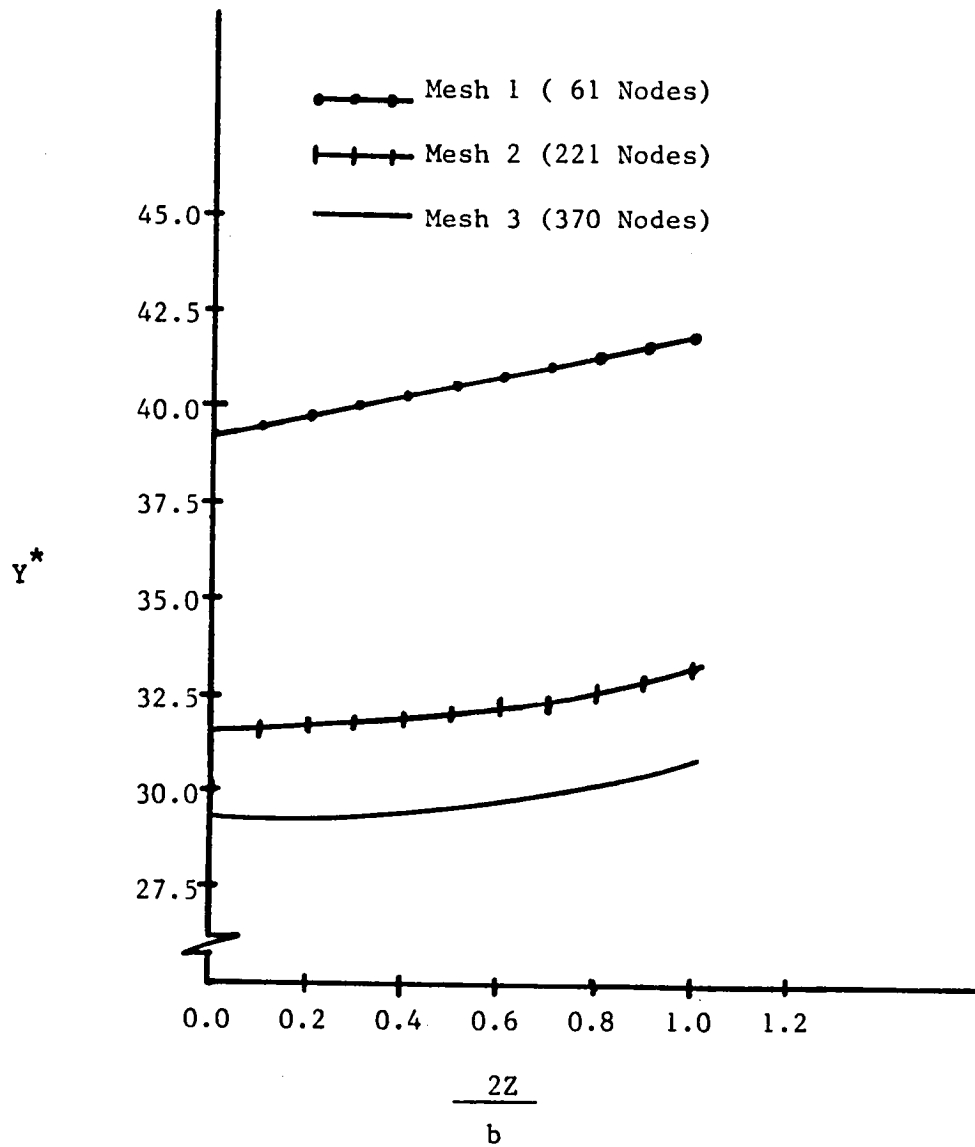


Figure 30. Variation of the stress intensity factor along the crack front for different mesh for $a/W = 0.5$

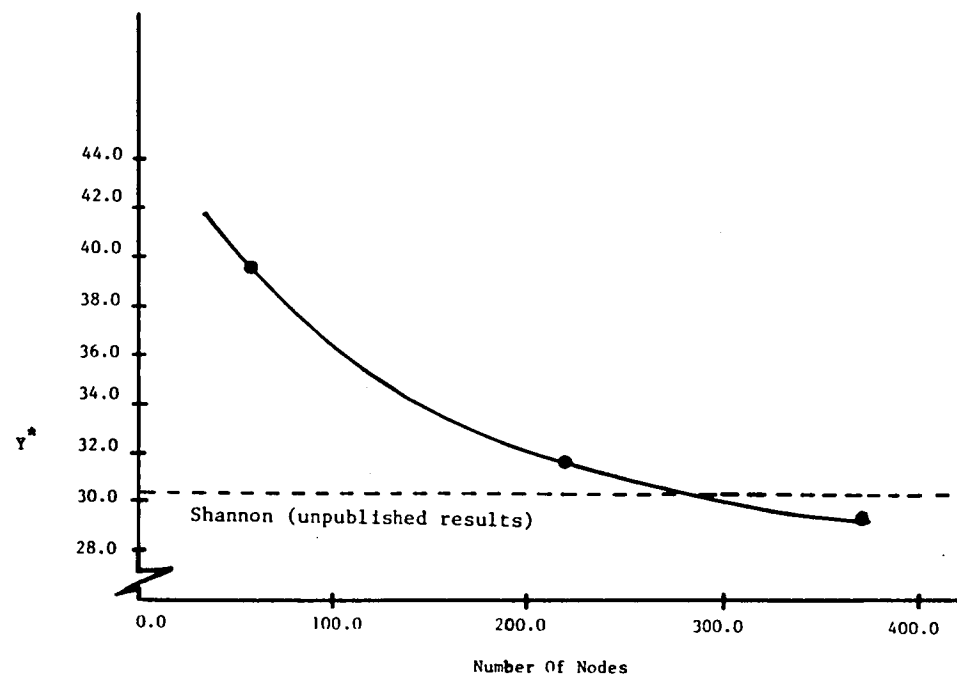


Figure 31. Variation of the stress intensity factor at the centerline of the specimen for $a/W = 0.5$ as function of the number of nodes

CHAPTER V

RESULTS AND DISCUSSION OF THE SHORT-BAR AND SHORT-ROD SPECIMENS

Normalized stress intensity factors Y^* and load line displacements for the Chevron-Notched short-rod and short-bar specimens are presented in this chapter. Two width-to-specimen thicknesses, equal to 1.45 and 2.00, were applied to both the short-rod and short-bar geometries. Therefore, four configurations are analyzed in this work. Table 3 gives a summary of the specimens dimensions used.

Table 3-- Summary of specimen dimensions.

specimen	W/B	a_0/W	a_1/W	H/B	X'/B
Short-bar	1.45	0.332	1.0	0.5	0.1
Short-bar	2.00	0.200	1.0	0.5	0.1
Short-rod	1.45	0.332	1.0	0.5	0.1
Short-rod	2.00	0.200	1.0	0.5	0.1

A uniform traction in the Z-direction, and triangularly

shaped in the X-direction was applied on all specimens (See Figure 19). The load was applied in a square groove cut into the specimens, 0.35 B height and 0.15 B deep (See Figure 18). A poisson's ratio of 0.333 was used.

Due to symmetry, only a quarter of the specimen was discretized into boundary segments. The number of segments and their geometries are similar to Mesh 3 described earlier (370 nodes and 420 boundary segments as shown in Figure 22). The boundary segments near the crack front have parabolic variation and linear variation everywhere else. No singularity elements are used in this study. For the short-rod specimens, the segments in $Y = 0.5$ plane as well as the segments in $Z = 0.5$ plane are combined together to form the cylindrical shape of the rod. The end view of the bar and rod configuration are shown in Figure 32. The rest of the planes have boundary segments meshes identical for both the short-bar and short-rod specimens.

Symmetric boundary conditions are applied in the $Z = 0$ plane, where the displacement in Z-direction is zero. For $Y = 0$ plane, the plane of the crack, all the segments are free except those that lie in the trapezoidal region where the displacement in the Y-direction is fixed. In order to prevent rigid-body-motion, only one node is fixed in the X-direction. For the short-bar specimen node 1 is fixed but for the short-bar specimen node 5 is fixed (Figure 32).

The stress intensity factor from compliance and displacement

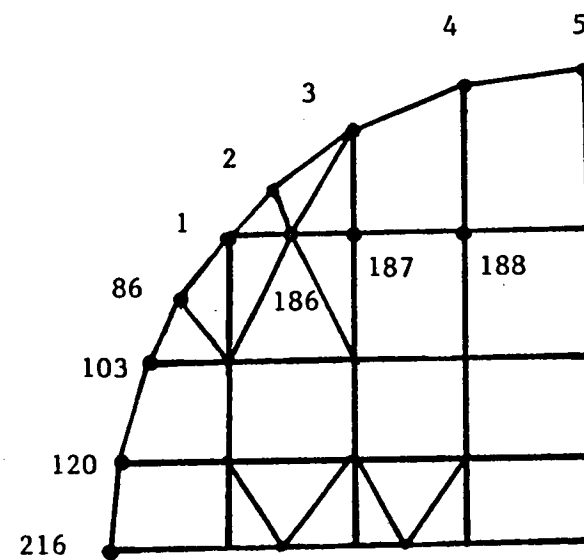
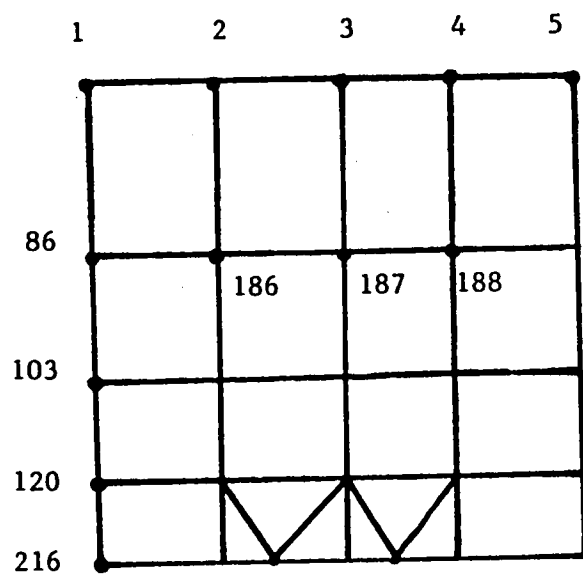


Figure 32. End-view of the short-bar and short-rod specimens

Table 4--NORMALIZED CRACK OPENING DISPLACEMENT FOR CHEVRON NOTCHED

SPECIMENS AS FUNCTION OF a/W a) EVB/P at center ($Z = 0$, $Y = 0.175$, $X = -a/W$)

Type	W/B	a/W						
		<u>0.35</u>	<u>0.40</u>	<u>0.50</u>	<u>0.55</u>	<u>0.60</u>	<u>0.70</u>	<u>0.75</u>
bar	1.45	60.73	67.72	92.68	110.26	129.37	197.37	261.28
bar	2.00	89.92	110.04	164.31	200.30	236.96	346.38	445.86
rod	1.45	82.29	94.92	129.27	153.93	186.91	274.99	348.52
rod	2.00	126.38	157.93	239.83	294.65	366.63	520.07	652.92

b) EVB/P at center ($Z = 0$, $Y = 0.5$, $X = -a/W$)

Type	W/B	a/W						
		<u>0.35</u>	<u>0.40</u>	<u>0.50</u>	<u>0.55</u>	<u>0.60</u>	<u>0.70</u>	<u>0.75</u>
bar	1.45	57.91	64.83	89.98	107.64	126.68	194.69	238.59
bar	2.00	87.12	107.31	161.70	197.73	234.29	343.62	443.07
rod	1.45	79.17	91.75	126.20	150.97	183.87	271.95	345.44
rod	2.00	123.22	154.85	236.86	291.73	363.84	516.87	649.66

fields are determined for five different crack-length positions. Since experimental results showed that a minimum stress intensity factor occurred between 0.5 and 0.6, the crack-length to specimen width ratios (a/W) used are $a/W = 0.40, 0.50, 0.55, 0.60, 0.70$. The mesh for a/W of 0.4 is given in Figure 22. The meshes for different a/W values are essentially the same except for the Y boundary condition in the plane of the crack, where one new layer is freed for each step increase in a/W .

5.1 STRESS INTENSITY FACTOR FROM COMPLIANCE

To determine the stress intensity factor from compliance, the displacement under the load line was determined for different crack-length positions using the BIE program. Table 4 gives the normalized displacements, $C^* = EVB/P$, at the midplane of the specimens, at $Y = 0.35 H$ and $Y = H$, assuming plane stress condition.

The displacement computed at $Y = H$, is always less than that at $Y = 0.35 H$. This variation has a maximum of 4.3% at $a/W = 0.4$ and a minimum of 1.4% at $a/W = 0.7$. Also note that this variation decreases with increasing W/B .

Since the analysis is performed under uniform loading conditions, a variation in the normalized displacement with Z along the loading line is computed. Table 5 shows some typical variations in the displacement between the center and the surface of the specimen.

Table 5--Typical variation of the displacement at the center
of the specimen to its outer surface along the loading line.

Type	W/B	a/W		
		<u>0.40</u>	<u>0.55</u>	<u>0.70</u>
Short-bar	1.45	-1.0%	-1.1%	-0.7%
Short-bar	2.00	-1.1%	-0.6%	-0.4%
Short-rod	1.45	7.3%	4.6%	3.3%
Short-rod	2.00	4.1%	2.3%	1.7%

Table 6--Normalized average displacement along the loading line,
EVB/P at $Y = 0.175$, $X = -a/W$

Type	W/B	a/W						
		<u>0.35</u>	<u>0.40</u>	<u>0.50</u>	<u>0.55</u>	<u>0.60</u>	<u>0.70</u>	<u>0.75</u>
Bar	1.45	60.28	67.08	92.09	109.76	128.61	196.83	261.07
Bar	2.00	89.35	109.41	163.76	199.88	236.14	345.86	445.53
Rod	1.45	83.82	96.40	130.91	157.94	188.79	277.29	350.91
Rod	2.00	127.67	159.34	241.36	296.16	368.36	522.14	655.26

As given in table 5, the displacement is not constant along the loading line. The displacements increase going from the center to the surface of the specimen for the short-rod and decrease for the short-bar. The percent variation is higher for the rod specimens. The variation decreases with increasing crack-length. For the same configuration the variation is lower for longer W/B.

Taking into consideration this variation along the loading line, an average displacement along the loading line was computed, and presented in Table 6. This average displacement was used in the determination of the stress intensity factor from compliance.

In determining the stress intensity factor, the average normalized compliance, $C^* = EVB/P$, is fitted in a polynomial. Since plots of compliance showed the appearance of exponentials, the polynomial used in the least square fit has the form:

$$\ln C^* = \ln \frac{EVB}{P} = d_1 + d_2 \alpha + d_3 \alpha^2 + d_4 \alpha^3$$

Table 7--Coefficients of the least square fit of the compliance.

Type	W/B	d_1	d_2	d_3	d_4
Short-bar	1.45	2.8362	5.147	-6.641	6.153
Short-bar	2.00	1.6743	12.518	-16.313	9.965
Short-rod	1.45	3.6014	2.064	0.484	1.029
Short-rod	2.00	2.7978	7.447	- 5.554	2.884

The coefficients of the least square fits of the normalized compliance are given in Table 7. Using these coefficients, the compliance's derivative for use in eq. (2.13) is found to be

$$\frac{d C^*}{d \alpha} = (d_2 + 2 d_3 \alpha + 3 d_4 \alpha^2). C^*$$

Having the values of the compliance's derivative, the normalized stress intensity factor was computed and plotted in Figure 33 as a function of α , assuming plane stress conditions. The values of the minimum normalized stress intensity factor Y^* and its position are given in Table 8.

Table 8--Critical stress intensity factor for the chevron notched specimens.

Type	W/B	(a/W) _m	Y _m [*]	A
Short-bar	1.45	0.529	23.675	19.661
Short-bar	2.00	0.516	28.328	20.031
Short-rod	1.45	0.543	29.097	24.164
Short-rod	2.00	0.492	36.246	25.630

A comparison between these minimum values and those presented at the ASTM Symposium on Chevron-Notched Specimens: Testing and Stress Analysis, with experimental results, is given in Table 9.

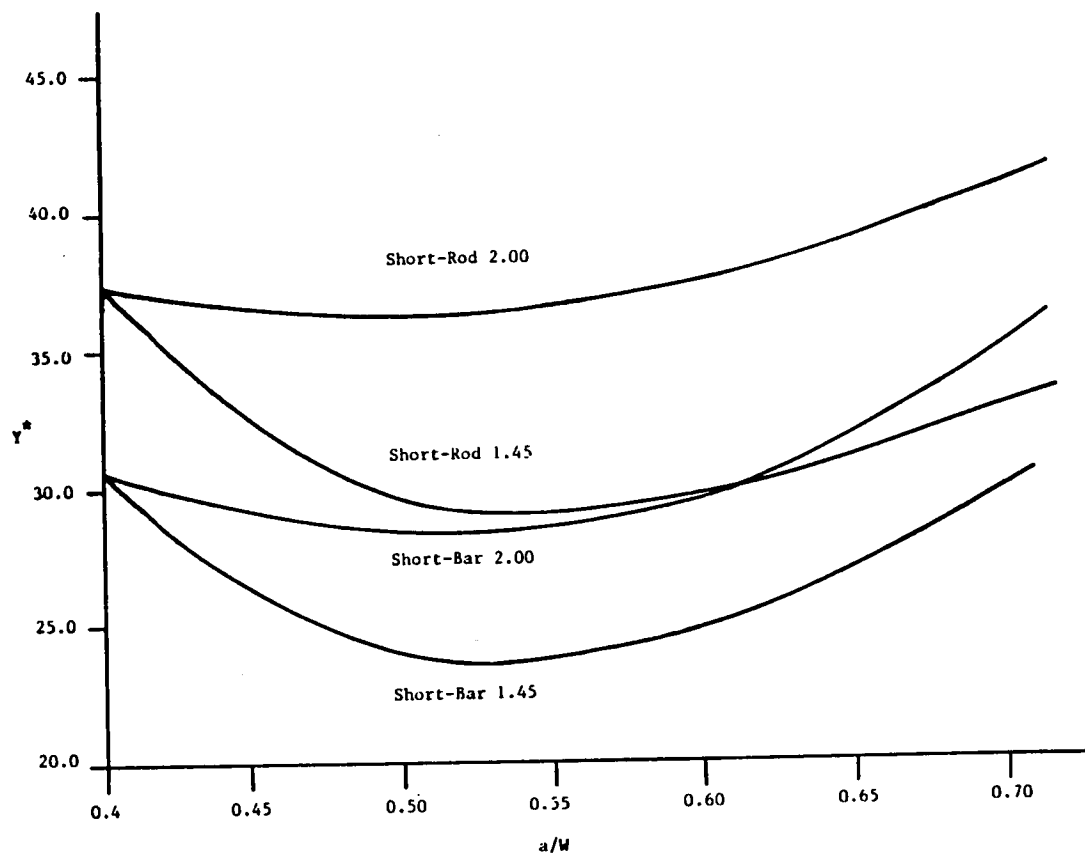


Figure 33. Stress intensity factor from compliance for the chevron-notched specimens as function of a/W

Table 9--Comparison between the minmum stress intensity factor
assuming plane stress condition

Type	a/w	BIE	FEM	EXP.	OTHER BIE
			Ref.[9]	Ref.[8]	
Bar	1.45	23.67	24.43	24.85	-----
Bar	2.00	28.33	29.13	29.91	27.81 Ref[10]
Rod	1.45	29.10	28.43	29.11	28.30 Ref[11]
Rod	2.00	36.25	35.40	36.36	-----

As seen in table 9, Using BIE, the critical Y^* for the short-bar specimens are 5% below experimental results compared with only 0.3% for the short-rod. On the other hand, the FEM results Ref.[9] are consistently 2.5% below experimental results.

5.2 Stress Intensity Factor Along The Crack Front.

Normalized stress intensity factors Y^* are computed point wise along the five crack fronts using the displacements obtained from BIE solutions. Plane strain condition is assumed along the entire crack front. The displacements divided by the square root of r , where r is the distance of the nodal point to the crack front, are plotted (Figure 29). As seen earlier these plots diverge as Z approaches the intersection of the crack front with the chevron notch, $Z = b/2$. This divergence is most severe for

Table 10--Stress Intensity Factor, Y^* , along the crack front
for the Short-Bar Specimens

a) $W/B = 1.45$

a/W	2Z/b					Av. Y^*
	<u>0.000</u>	<u>0.500</u>	<u>0.750</u>	<u>0.875</u>	<u>1.000</u>	
0.40	30.97	31.03	31.13	31.20	31.29	31.07
0.50	28.69	28.94	29.22	29.41	29.65	29.03
0.55	29.02	29.30	29.59	29.78	30.02	29.39
0.60	29.79	30.22	30.69	31.01	31.43	30.38
0.70	36.73	37.15	37.49	37.75	38.05	37.24

b) $W/B = 2.00$

a/W	2Z/b					Av. Y^*
	<u>0.000</u>	<u>0.500</u>	<u>0.750</u>	<u>0.875</u>	<u>1.000</u>	
0.40	29.79	30.35	30.94	31.32	31.79	30.53
0.50	29.28	29.76	30.22	30.53	30.93	29.90
0.55	29.88	30.29	30.62	30.84	31.01	30.36
0.60	30.10	30.54	30.85	31.15	31.57	30.63
0.70	34.29	34.78	34.94	35.23	35.79	34.81

Table 11--Stress Intensity Factor, Y^* , along the crack front
for Short-Rod Specimens.

a) $W/B = 1.45$

a/W	$2Z/b$					Av. Y^*
	<u>0.000</u>	<u>0.500</u>	<u>0.750</u>	<u>0.875</u>	<u>1.000</u>	
0.40	37.39	37.47	37.59	37.65	37.76	37.51
0.50	33.35	33.56	33.75	33.89	34.05	33.62
0.55	33.29	33.44	33.52	33.58	33.67	33.45
0.60	34.95	35.15	35.23	35.32	35.49	35.16
0.70	40.96	40.72	40.09	39.73	39.35	40.45

b) $W/B = 2.00$

a/W	$2Z/b$					Av. Y^*
	<u>0.000</u>	<u>0.500</u>	<u>0.750</u>	<u>0.875</u>	<u>1.000</u>	
0.40	38.60	39.21	39.79	40.17	40.67	39.38
0.50	37.96	38.29	38.48	38.61	38.82	38.32
0.55	38.84	38.95	38.80	38.71	38.65	38.85
0.60	40.81	40.79	40.35	40.14	40.06	40.59
0.70	44.67	44.19	42.76	42.01	41.38	43.51

very short crack widths, b . This is due to the inadequacy of modelling the intersection of the two cracks. For this reason, only the nodes greater than 0.1 are fitted in a linear equation to determine the intercept of that curve at $r = 0.0$, as discussed in section 2.5.

The distribution of the Y^* along the crack front for the bar and rod configurations are given in Tables 10 and 11. Figures 34 and 35 represent the variation of the short bar along the crack front, for various a/W ratios. All those distributions show that the minimum Y^* occurs at the center and that the highest values are at $Z = b/2$. For the short-bar with $W/B = 2.00$, the highest difference of Y^* between $Z = 0.0$ and $Z = b/2$, is for small values of a/W . For the short-rod configuration the variation along the crack front is similar to the bar with the lowest Y^* at the center for low a/W values. But as a/W increases the reverse is true. This reverse effect occurs at $a/W = 0.7$ for the the rod with $W/B = 1.45$, while for $W/B = 2.00$ this reverse effect occurs at $a/W = 0.55$ but still at the same crack width ($b/B = 0.55$), as seen in Figures 36 and 37. This effect was also observe by Ingraffea et al. in Ref. [11]. A sequence of his photographs, which are reproduced here in Figure 38, show that for small crack lengths the propagation at the centerline is relatively retarded since Y^* is lowest at that position. The crack front gradually straightens and ultimately, thumbnails. Figures 36 and 37 of Y^* of the short-rod specimens predict the same effect. In contrast,

the FEM solutions [9] and the BIE solutions [11], both using \sqrt{r} singularity elements near the crack front did not predict this thumbnailing effect.

A comparison between Y^* from compliance and the average Y^* along the crack front, shows that the compliance Y^* is always lower than the average Y^* (see Tables 10 and 11). For specimens with $W/B = 2.00$, show about 5% difference. But for $W/B = 1.45$ the difference is much higher, about 20% . This difference is partly due to the divergence of V/\sqrt{r} for small crack widths. Eventhough the magnitudes of Y^* are different, the positions of the minimum Y^* are in good agreement for both methods.

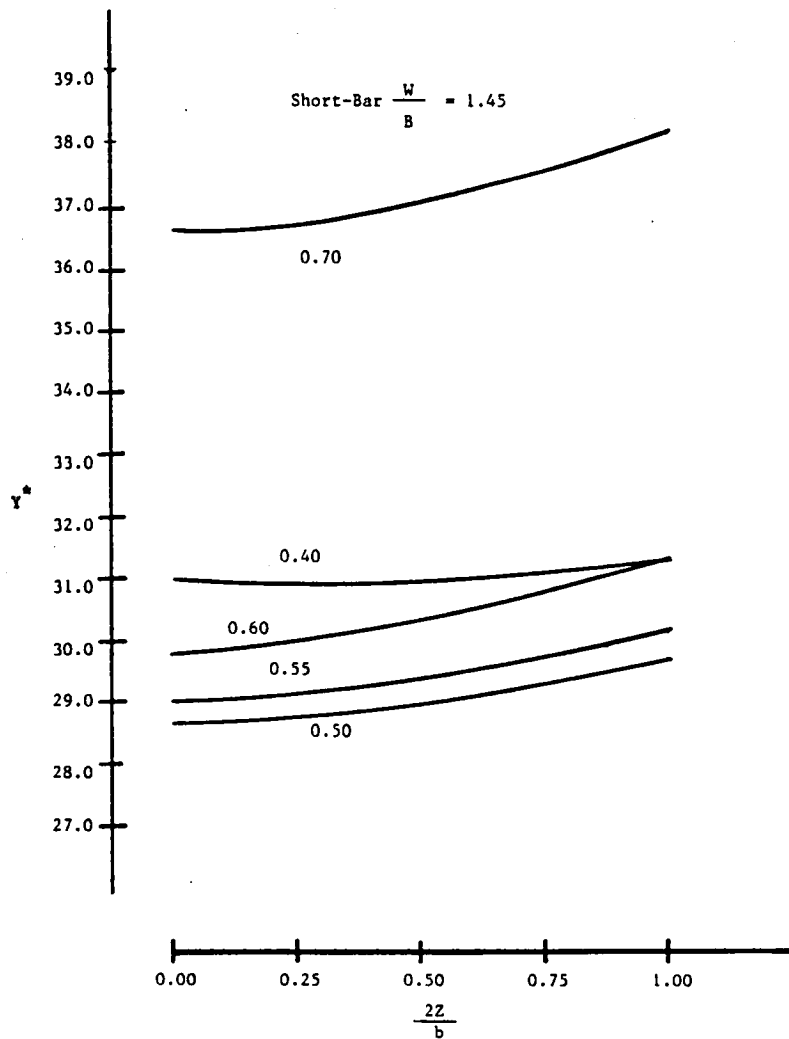


Figure 34. Variation of the stress intensity factor along the crack front of the short-bar specimen with $W/B = 1.45$

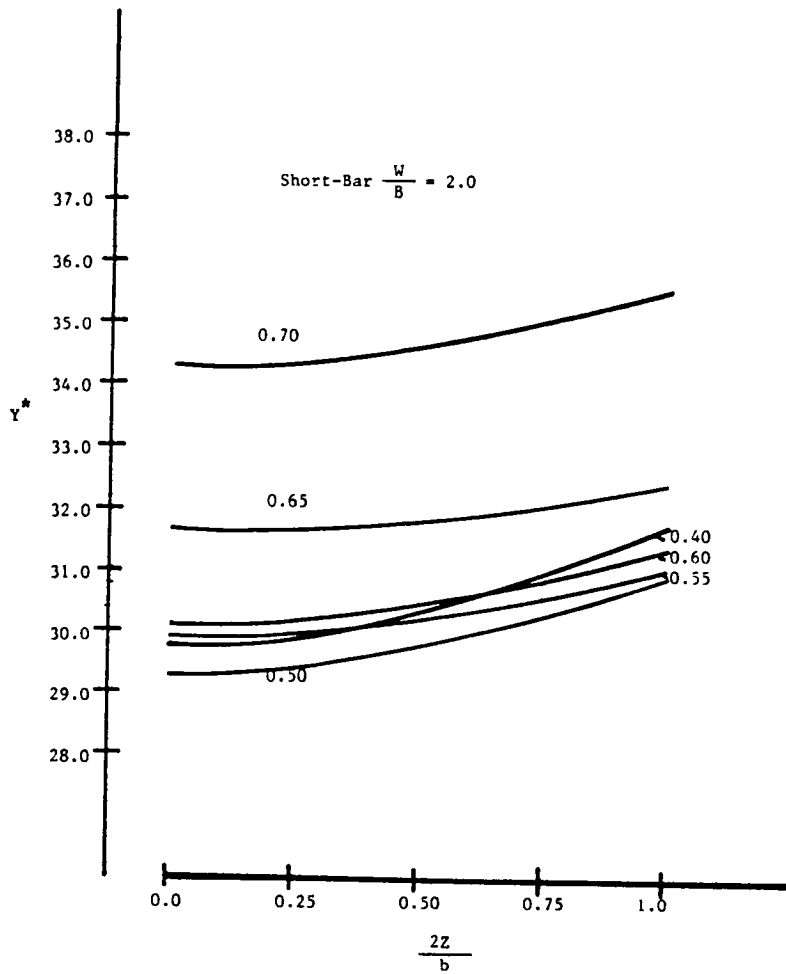


Figure 35. Variation of the stress intensity factor along the crack front of the short-bar specimen with $W/B = 2.00$

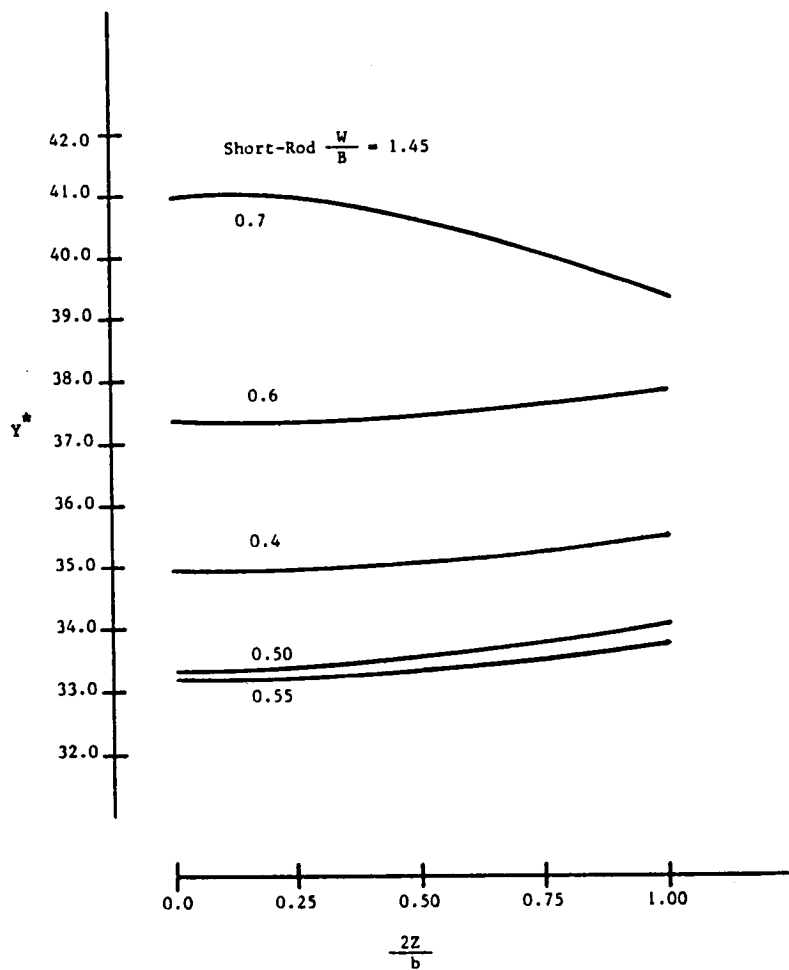


Figure 36. Variation of the stress intensity factor along the crack front of the short-rod specimen with $W/B = 1.45$

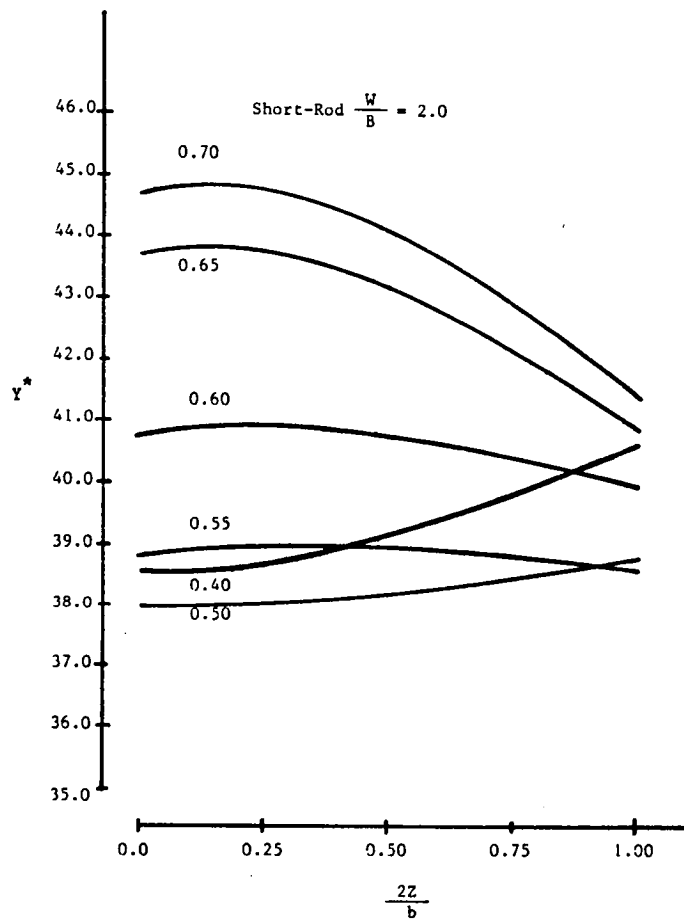


Figure 37. Variation of the stress intensity factor along the crack front of the short-rod specimen with $W/B = 2.00$

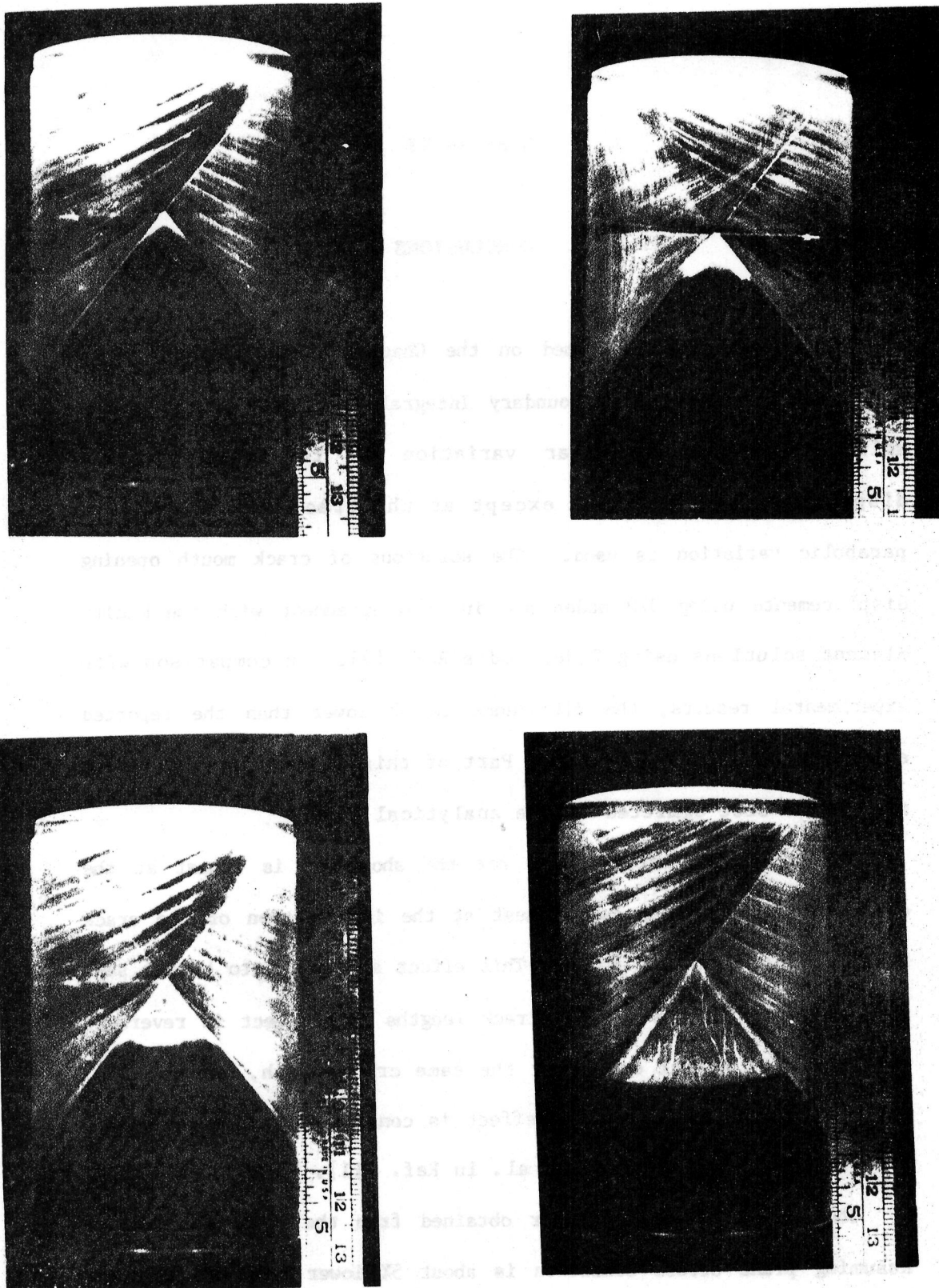


Figure 38. Propagation of the crack front for the short-rod specimen
Ref. [11]

CHAPTER VI

CONCLUSIONS

An analysis was performed on the Chevron-Notched Short-Bar and Short-Rod specimens using Boundary Integral Equations Method. This solution assumes a linear variation of the tractions and displacements everywhere except at the crack front, where a parabolic variation is used. The solutions of crack mouth opening displacements using 370 nodes are in good agreement with the Finite Element solutions using 2,960 nodes Ref. [9]. In comparison with experimental results, the difference is 4% lower than the reported experimental values Ref. [8]. Part of this discrepancy is due to the finite slot omitted in the analytical model.

The stress intensity factor for the short-bar is lowest at the center of the specimen and highest at the intersection of the crack front with the chevron notch. This effect starts out to be the same for the short-rod but at high crack lengths this effect is reversed. This reversal effect occurs at the same crack width, $b/B = 0.55$, for both values of W/B . This effect is consistent with experimental results shown by Ingraffea et al. in Ref. [11].

The stress intensity factor obtained from the compliance method assuming plane stress condition is about 5% lower than the reported

experimental values from Ref. [8], for the short-bar specimens. For the short-rod specimens the agreement is much better, having less 0.3% difference.

There is some difference for both the rod and bar specimens with $W/B = 1.45$ between the compliance Y^* and the average Y^* along the crack front. For $W/B = 1.45$ the difference for large a/W is around 20% . For $W/B = 2.00$ the difference is less than 5% between the two methods.

The minimum stress intensity factors are reported in Table 8. The minimum position is between 0.49 and 0.55 for all chevron-notched configurations analysed. These positions agree well with the minimum stress intensity factor along the crack front eventhough the magnitudes of Y^* are different.

As a conclusion, the Boundary Integral Equations method has a great potential in solving fracture mechanics problems. Improvements could be incorporated by using higher order variation of the tractions and displacements in each surface segment instead of the linear variation currently used. Also a \sqrt{r} singularity near the crack front could improve the solution of the stress intensity factors along the crack front. As for the Chevron-Notched Specimens, the effect of the intersection of the crack front with the chevron notch should be analysed in greater detail to determine the exact singularity in this region.

REFERENCES

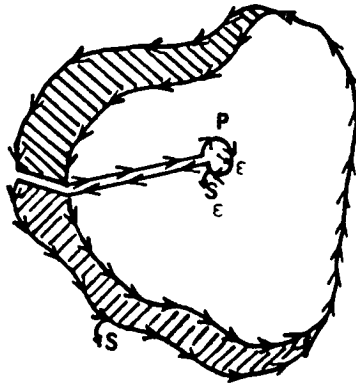
1. Paris, P.C. and Sih, G.C., Stress Analysis of Cracks, ASTM STP 381, (1965) pp. 30-81
2. Barker, L.M., "A Simplified Method for Measuring Plane Strain Fracture Toughness", Engineering Fracture Mechanics, vol. 9, (1977), pp. 361-369.
3. Barker, L.M., "Short Bar Specimens for K_{IC} Measurements", American Society for Testing and Materials, ASTM STP-678, (1979), pp. 73-82.
4. Barker, L.M., "Compliance Calibration of a Family of Short-Rod and Short-Bar Fracture Toughness Specimens", Engineering Fracture Mechanics, vol. 17, No. 4, (1983), pp. 289-312.
5. Barker, L.M., and Guest, R.V., " Compliance Calibration of the short rod Fracture Toughness Specimen", Terra Tek Report TR 78-20, 1978.
6. Munz, D., Bubsey, R.T. and Srawley, J.E., "Compliance and Stress Intensity Coefficients for Short Bar Specimens with Chevron Notches Useful for Fracture Toughness Testing of Ceramics", International Journal of Fracture, vol. 16, No. 4, (1980), pp. 359-374.
7. Bubsey, R.T., Munz, D., Pierce, W.S. and Shannon, J.L., Jr., "Compliance Calibration of the Short Rod Chevron-Notch Specimen for Fracture Toughness Testing of Brittle Materials" International Journal of Fracture, vol. 18, No. 1, (1982), pp. 125-132.
8. Shannon, J.L., Jr., Bubsey, R.T., Pierce, W.S. and Munz, D., "Extended Range Stress Intensity Factor Expressions for Chevron-Notched Short Bar and Short Rod Fracture Toughness", International Journal of Fracture, vol. 19, No. 3, (1982) pp. R55-R58.
9. Raju, I.S. and Newman, J.C., Jr., "Three-Dimensional Finite-Element Analysis of the Chevron-Notched Fracture Specimens", presented at the ASTM Symposium of Chevron-Notched Specimens: Testing and Stress Analysis, Louisville, Ky., April, 1983.
10. Mendelson, A. and Ghosn, L.J., "Three-Dimensional Analysis of Short-Bar Chevron-Notched Specimens by Boundary Integral Method", presented at the ASTM Symposium on Chevron-Notched Specimens: Testing and Stress Analysis, Louisville, Ky., April 1983.

11. Ingraffea, A.R., Perucchio, R., Han, T.Y., Grestle, W.H. and Huang, Y.P., "Three-Dimensional Finite and Boundary Element Calibration of the Short-Rod Specimen", presented at the ASTM Symposium on Chevron-Notched Specimens: Testing and Stress Analysis, Louisville, Ky., April, 1983.
12. Tattersal, H.G. and Tappin, G., "The Work of Fracture and its Measurements in Metals, Ceramics and other Materials", Journal of Materials Science, 1, (1966), pp. 296-301.
13. Love, A.E.H., A treatise on the Mathematical Theory of Elasticity, Dover, N.Y., 1944.
14. Sokolnikoff, I.S., Mathematical Theory of Elasticity, McGraw-Hill, New York, 1956.
15. Mendelson, A., "Boundary-Integral Methods in Elasticity and Plasticity", NASA TND-7418, National Aeronautics and Space Administration, Washington, D.C., November, 1973.
16. Raju, I.S. and Newman, J.C., Jr., "Three-Dimensional Finite-Element Analysis of Finite-Thickness Fracture Specimens", NASA TND-8414, National Aeronautics and Space Administration, Washington, D.C., May, 1977.
17. Mendelson, A. and Alam, J., "The Use of the Method of Lines in 3-D Fracture Mechanics Analysis with Application to Compact Tension Specimens", International Journal of Fracture, vol.22, (1983), pp. 105-116.
18. Cruse, T.A., "An Improved Boundary-Integral Equation Method For Three Dimensional Elastic Stress Analysis", Computers and Structures, vol. 4, (1974), pp.741-754.
19. Cristesou, M. and Loubignac, G., Advances in Boundary Element Methods, C.A. Brebbia. Ed., Pentech Press, London, 1978, pp.375-389.
20. Rizzo, F.J. "An Integral Equation Approach to Boundary Value Problems of Classical Elastostatics", Quarterly of Applied Mathematics, vol. 25, (1967), pp.83-95.

APPENDIX A

Derivation of the Singular Integral

Because of the singular nature of Kelvin's solution a surface cut is made in the body to exclude the point P from the region (where U_{ij} and $T_{ij} \rightarrow \infty$).



The surface integral going from the surface boundary to the singularity point P is cancelled by the integral coming back since it can be considered that the same path is being integrated over but in opposite direction, therefore Betti's theorem (3.7) will have the form:

$$\int_S t_j U_{ij} ds + \int_{S_\epsilon} t_j U_{ij} ds_\epsilon = \int_S u_j T_{ij} ds + \int_{S_\epsilon} u_j T_{ij} ds_\epsilon \quad (A.1)$$

where s is the boundary surface of the body and s_ϵ is the surface of a sphere of radius ϵ which excludes the singularity

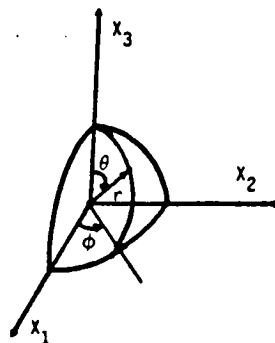
point of U_{ij} and T_{ij} .

Considering the value of the integral at point P as the radius of s_ϵ goes to zero ($\epsilon \rightarrow 0$) , and noting that :

$$ds = \epsilon^2 \sin\theta \, d\theta \, d\phi$$

$$r_{,i} = n_i$$

$$\bar{n} = \begin{pmatrix} -\sin\theta \cos\phi \\ -\sin\theta \sin\phi \\ -\cos\theta \end{pmatrix}$$



$$\frac{dr}{dn} = 1 ; \quad r_{,i} n_j - r_{,j} n_i = 0$$

The values of the integrals around s_ϵ can be evaluated as follows:

Substituting the value of U_{ij} from equation (3.2)

$$\iint_{s_\epsilon} t_j U_{ij} \, ds_\epsilon = \int_0^{2\pi} \int_0^\pi \frac{1}{4\pi G} \frac{1}{\epsilon} \left[\frac{3-4\nu}{4(1-\nu)} \delta_{ij} + \frac{1}{4(1-\nu)} \epsilon_{,i} \epsilon_{,j} \right] t_j \epsilon^2 \sin\theta \, d\theta \, d\phi$$

Putting ϵ outside the integral:

$$= \epsilon \int_0^{2\pi} \int_0^\pi \frac{1}{16 G(1-u)} (3-4u) \delta_{ij} + n_i n_j \quad t_j \sin \theta \, d\theta \, d\phi$$

and taking the limit as $\epsilon \rightarrow 0$,

$$\lim_{\epsilon \rightarrow 0} \iint_{S_\epsilon} t_j U_{ij} \, ds = 0 \quad (A.2)$$

by substituting equation (3.6) for T_{ij} , the second integral

becomes:
$$\iint_{S_\epsilon} u_j T_{ij} \, ds_\epsilon = \int_0^{2\pi} \int_0^\pi \frac{-(1-2u)}{8\pi(1-u)} \quad$$

$$\frac{u_j}{\epsilon} \left\{ \frac{d\epsilon}{dn} \left[\delta_{ij} + \frac{3}{1-2u} \epsilon_{,i} \epsilon_{,j} \right] \right\} \epsilon^2 \sin \theta \, d\theta \, d\phi$$

$$= \int_0^{2\pi} \int_0^\pi \frac{-(1-2u)u_j}{8\pi(1-u)} \left[\delta_{ij} + \frac{3}{1-2u} n_i n_j \right] \sin \theta \, d\theta \, d\phi$$

Evaluating the function in matrix form:

$$\delta_{ij} + \frac{3}{1-2u} n_i n_j = \begin{Bmatrix} 1 + \frac{3}{1-2u} \sin^2 \theta \cos^2 \phi & \sin^2 \theta \cos \phi \sin \phi & \sin \theta \cos \theta \cos \phi \\ \sin^2 \theta \cos \phi \sin \phi & 1 + \frac{3}{1-2u} \sin^2 \theta \sin^2 \phi & \sin \theta \cos \theta \sin \phi \\ \sin \theta \cos \theta \cos \phi & \sin \theta \cos \theta \sin \phi & 1 + \frac{3}{1-2u} \cos^2 \theta \end{Bmatrix}$$

Integrating each term of the matrix, the above equation gives:

$$\int_0^{2\pi} \int_0^\pi \frac{-(1-2\nu)u_j}{8\pi(1-\nu)} \left[\delta_{ij} + \frac{3}{1-2\nu} n_i n_j \right] \sin\theta d\theta d\phi = -\delta_{ij} u_j \quad (\text{A.3})$$

By substituting relation (A.2) and (A.3) in equation (A.1) one gets the boundary integral equations :

$$\int_s t_j u_{ij} ds = \int_s u_j T_{ij} ds - \delta_{ij} u_j \quad (\text{A.4})$$

If the point P is at the surface of the body s_ϵ would be a surface of half a sphere. The above equations integrated over half the sphere are equal to

$$\lim_{\epsilon \rightarrow 0} \int_{s_\epsilon} t_j u_{ij} ds = 0$$

$$\lim_{\epsilon \rightarrow 0} \int_{s_\epsilon} u_j T_{ij} ds = \frac{1}{2} \delta_{ij} u_j$$

so Betti's theorem will be equal to

$$\int_s t_j u_{ij} ds = \int_s u_j T_{ij} ds - \frac{1}{2} \delta_{ij} u_j \quad (\text{A.5})$$

or in general

$$\int_s t_j u_{ij} ds = \int_s u_j T_{ij} ds - C_{ij} u_j$$

where $C_{ij} = \delta_{ij}$ for internal points, and $C_{ij} = \frac{1}{2} \delta_{ij}$ for surface points.

APPENDIX B

Numerical Solution of the Integral Equations

General analytical solutions to the integral equations are not available and it is therefore necessary to solve the equations numerically. The integral equations have the form:

$$\begin{aligned} C_{ij}(P) u_j(P) + \int_s T_{ij}(P,Q) u_j(Q) ds(Q) \\ = \int_s U_{ij}(P,Q) t_j(Q) ds(Q) \end{aligned}$$

where u_j and t_j are the displacement and the stress vectors respectively, P is the source point indicating the location at which the force acts, and Q is the field point denoting the actual boundary point.

The integrals are Cauchy Principal Value Integrals where $C_{ij}(P)$ is a field of constants depending on the smoothness of boundary in P . $C_{ij}(P)$ is equal $1/2 \delta_{ij}$ if P is at a smooth surface. For the case where P is at an edge or a corner [18],

$$C_{ij}(P) = -\sum \int_s T_{ij}(P,Q) ds(Q) \quad . \quad \text{for } P \neq Q$$

The numerical solution for the integral equations are found by discretizing the boundary into segments. In the computer

program used in the present work, the surface is represented by triangular and rectangular elements. The traction and displacement inside each element are linear functions of the traction and displacement at each corner.

For triangular element

$$t_i(\xi) = C^k(\xi) t_i^k$$

$$u_i(\xi) = C^k(\xi) u_i^k$$

where from Ref.[18]

$$C^k(\xi) = \frac{1}{3} + (F_{k2} \xi_{1m} - F_{k1} \xi_{2m})/2S - (F_{k2} \xi_1 - F_{k1} \xi_2)/2S$$

ξ_1, ξ_2 are local in-plane coordinates of the field point Q, ξ_{1m}, ξ_{2m} are local in-plane coordinates of the centroid of the m th element. F_{K1}, F_{K2} are the projections of the distance between two adjacent nodes in local coordinates and $K = 1, 2, 3$.

For rectangular elements

$$t_i(\xi) = N^k(\xi) t_i^k$$

$$u_i(\xi) = N^k(\xi) u_i^k$$

where

$$\begin{aligned} N^1 &= \frac{(1 - \xi_1)(1 - \xi_2)}{4} & N^2 &= \frac{(1 + \xi_1)(1 - \xi_2)}{4} \\ N^3 &= \frac{(1 + \xi_1)(1 + \xi_2)}{4} & N^4 &= \frac{(1 - \xi_1)(1 + \xi_2)}{4} \end{aligned}$$

If the surface is represented by m triangular elements and n rectangular elements the equations become:

$$\begin{aligned} & C_{1j}(P) u_j(P) + \sum_{b=1}^m \sum_{K=1}^3 u_j(Q^{bK}) \int_{\Delta S} T_{1j}(P, Q) C^K(\xi) J(\xi) d\xi \\ & + \sum_{b=1}^n \sum_{K=1}^4 u_j(Q^{bK}) \int_{\Delta S} T_{1j}(P, Q) N^K(\xi) J(\xi) d\xi \\ & = \sum_{b=1}^m \sum_{K=1}^3 t_j(Q^{bK}) \int_{\Delta S} U_{1j}(P, Q) C^K(\xi) J(\xi) d\xi \\ & + \sum_{b=1}^n \sum_{K=1}^4 t_j(Q^{bK}) \int_{\Delta S} U_{1j}(P, Q) N^K(\xi) J(\xi) d\xi \end{aligned}$$

where $J(\xi)$ is the well known Jacobi function. The terms $u_j(Q^{bK})$ or $t_j(Q^{bK})$, respectively, are the corner values of displacements and tractions of the k th node within the b th element.

For $Q^{bK} \neq P$, a 4×4 Gaussian quadrature formula is used to evaluate numerically the integration.

For $Q^{bK} = P$, in a triangular element the integrals are evaluated in closed form by a change to cylindrical coordinates (r, θ) , [18].

$$\begin{aligned} & \lim_{\epsilon \rightarrow 0} \int_{\theta_1}^{\theta_2} \int_{\epsilon}^r T_{ij}(P, Q) C^K(\xi) J(\xi) d\xi \\ & \lim_{\epsilon \rightarrow 0} \int_{\theta_1}^{\theta_2} \int_{\epsilon}^r U_{ij}(P, Q) C^K(\xi) J(\xi) d\xi \end{aligned}$$

But, for rectangular elements a special singular Gauss quadrature is used derived in reference [19] for an integral with $1/r$ singularity.

When the integrals are calculated for P at a node, then C_{ij} (P) is obtained by summing the $\int_s T_{ij} ds$ terms.

Then the integral equations result in a system of $3 \times (m + n)$ linear algebraic equations to be solved for the unknown boundary tractions or displacements.

The use of both triangular and rectangular elements is necessitated due to the use of a fine mesh near the crack front and a coarse mesh further away. The triangular elements are thus used as transition elements.

1. Report No. NASA CR-172225		2. Government Accession No.		3. Recipient's Catalog No.	
4. Title and Subtitle THREE-DIMENSIONAL ANALYSIS OF CHEVRON-NOTCHED SPECIMENS BY BOUNDARY INTEGRAL METHOD				5. Report Date September 1983	
				6. Performing Organization Code	
7. Author(s) Alexander Mendelson and Louis Ghosn				8. Performing Organization Report No.	
9. Performing Organization Name and Address Case Western Reserve University Department of Civil Engineering Cleveland, OH 44106				10. Work Unit No.	
				11. Contract or Grant No. NAG-1-304	
12. Sponsoring Agency Name and Address National Aeronautics and Space Administration Washington, DC 20546				13. Type of Report and Period Covered Contractor Report	
				14. Sponsoring Agency Code	
15. Supplementary Notes Langley Technical Monitor: J. C. Newman, Jr. Final Report					
16. Abstract A three-dimensional elastic analysis was performed on the chevron-notched short-bar and short-rod specimens, using the boundary integral equations method. This method makes use of boundary surface elements in obtaining the solution. The boundary integral models were composed of linear triangular and rectangular surface segments. Results were obtained for two specimens with width-to-thickness ratios of 1.45 and 2.00 and for different crack-length-to-width ratios ranging from 0.4 to 0.7. Crack opening displacement and stress intensity factors determined both from displacement calculations along the crack front and compliance calculations were compared with experimental values obtained at NASA Lewis Research Center, and with finite-element analysis done at NASA Langley Research Center.					
17. Key Words (Suggested by Author(s)) Fracture mechanics Ceramics Displacements Stress intensity factors Boundary-integral method				18. Distribution Statement Unclassified - Unlimited Subject Category 39	
19. Security Classif. (of this report) Unclassified		20. Security Classif. (of this page) Unclassified		21. No. of Pages 107	
				22. Price* A06	

